THE ANATOMICAL RECORD 303:1768–1791 (2020)

Computational Fluid Dynamics Reveals a Unique Net Unidirectional Pattern of Pulmonary Airflow in the Savannah Monitor Lizard (*Varanus exanthematicus*)

ROBERT L. CIERI* AND C.G. FARMER
School of Biological Sciences, University of Utah, Salt Lake City, Utah

This report models pulmonary airflow in the savannah monitor (*Varanus exanthematicus*) using computational fluid dynamics simulations, which are based on computed tomography data. Simulations were validated by visualizing the flow of aerosolized lipids in excised lungs with good but not perfect agreement. The lung of this lizard has numerous successive bronchi branching off a long intrapulmonary bronchus, which are interconnected by intercameral perforations. Unidirectional flow has been documented in the lateral secondary bronchi of the savannah monitor, but patterns of airflow in the rest of the lung remain unknown, hindering our understanding of the evolution of pulmonary patterns of airflow in tetrapods. These results indicate that the lung contains a unique net unidirectional flow, where the overall flow scheme is similar during expiration and late inspiration, but dissimilar during early inspiration. Air is transported net caudally through the intrapulmonary bronchus and net craniad through secondary bronchi, much like the pattern of flow in birds. The simulations show that many chambers feature flow in multiple directions during parts of the respiratory cycle, but some regions also show robust unidirectional airflow. Air moves craniad through secondary bronchi and between adjacent secondary bronchi through intercameral perforations. The first secondary bronchus, the hilar-cranial bronchus, contains tidal flow that may improve ventilation of the central and dorsal lung parenchyma. These results expand our understanding of flow patterns in varanid lungs and suggest lungs with net unidirectional flow as an evolutionary pathway between tidal flow and complete unidirectional flow in multicameral lungs. Anat Rec, 303:1768–1791, 2020. © 2019 American Association for Anatomy

This article includes AR WOW Videos. Video 1 can be viewed at: https://players.brightcove.net/656326989001/default_default/index.html?videoId=6115073507001. Video 2 can be viewed at: https://players.brightcove.net/656326989001/default_default/index.html?videoId=6115074896001. Video 3 can be viewed at: https://players.brightcove.net/656326989001/default_default/index.html?videoId=6115075633001. Video 4 can be viewed at: https://players.brightcove.net/656326989001/default_default/index.html?videoId=6115073199001. Video 5 can be viewed at: https://players.brightcove.net/656326989001/default_default/index.html?videoId=6115072712001. Video 6 can be viewed at: https://players.brightcove.net/656326989001/default_default/index.html?videoId=6115073506001. Video 7 can be viewed at: https://players.brightcove.net/656326989001/default_default/index.html?videoId=6115073632001. Video 8 can be viewed at: https://players.brightcove.net/656326989001/default_default/index.html?videoId=6098782189001. Video 9 can be viewed at: https://players.brightcove.net/656326989001/default_default/index.html?videoId=6098782188001.

Grant sponsor: Division of Integrative Organismal Systems; Grant number: 1055080; Grant sponsor: National Science Foundation; Grant numbers: 1747505, ACI-1238993, OCI-0725070.

*Correspondence to: Robert L. Cieri, School of Biological Sciences, University of Utah, 247 S 1400 E, 201 South Biology, Salt Lake City, UT 84108. Tel: 801-585-7756, Fax: 801-581-4668

E-mail: bob.cieri@gmail.com

Received 2 May 2019; Revised 4 October 2019; Accepted 7 October 2019.

DOI: 10.1002/ar.24293
Published online 13 December 2019 in Wiley Online Library (wileyonlinelibrary.com).

Key words: ventilation; pulmonary; varanidae; computational fluid dynamics; unidirectional airflow

INTRODUCTION

The lungs of monitor lizards (Varanidae) are complex structures that have long fascinated biologists. Their anatomy is qualitatively reminiscent of avian lungs, featuring a long intrapulmonary bronchus, and saccular regions surrounding a dense, central parenchyma (Wolf, 1933; Kirschfeld, 1970; Schachner et al., 2013b). Intercameral perforations between secondary bronchi make it possible for air to take multiple routes through the lung (Wolf, 1933; Schachner et al., 2013b), raising interesting questions about the evolution of lung design and pulmonary airflow in vertebrates (Farmer, 2015a; Cieri and Farmer, 2016). Unidirectional airflow has been discovered in one part of monitor lungs (Schachner et al., 2013b), but how air flows through the majority of the lung chambers and the fluidic mechanisms that underpin these patterns of flow remain largely unknown. Computational fluid dynamics (CFD) modeling, which simulates fluid flow using the equations of fluid transport, is an exciting tool for investigating patterns of airflow through lungs and promises to help us understand mechanistically these patterns of flow, as well as to reconstruct the evolution of pulmonary patterns of airflow in vertebrates (Fig. 1).

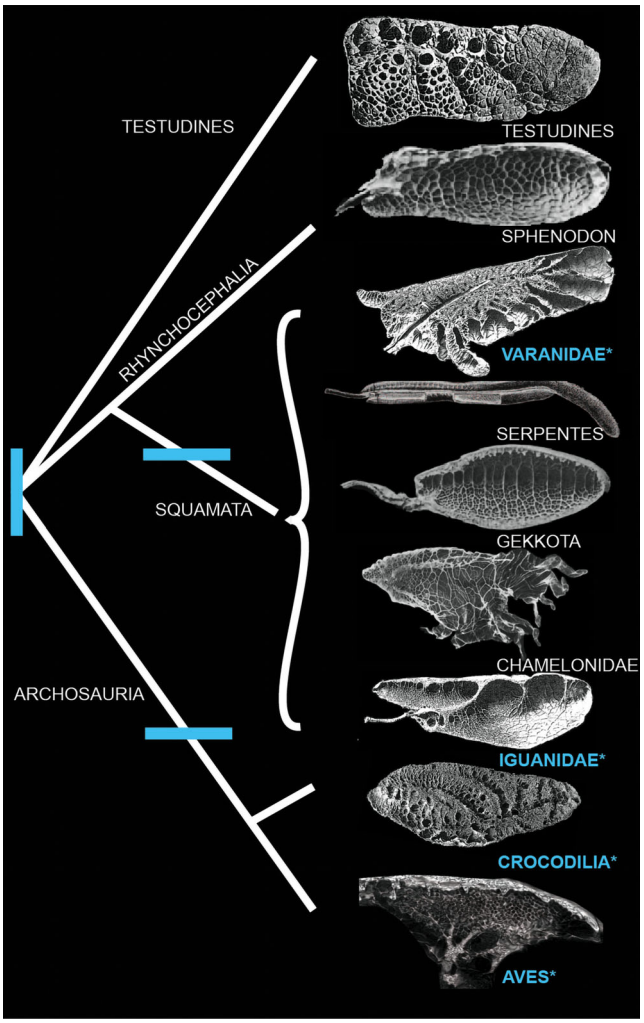

Fig. 1. Cladogram of reptiles illustrating some of the diversity of pulmonary morphology and the evolution of unidirectional pulmonary airflow. Taxa where unidirectional airflow have been documented are in bold blue and indicated with an asterisk. The presence of unidirectional airflow in squamates and archosaurs may suggest that this trait is basal to Diapsida (vertical blue bar), but it could also have evolved independently in squamates and archosaurs. Reprinted by permission from Cieri and Farmer, J Comp Physiol B, 2016, 186, 541–552. Images adapted from Milani, Zool Jahrbucher, 1894, 10, 93–146. The cladogram is a compromise between (Lee, 2001; Chiari et al., 2012; Lyson et al., 2012).

The study of varanid lungs has a long history. Milani (1894) first sketched their unique morphology, including the cranial and caudal saccular regions, intrapulmonary bronchus, and other bronchi dorsal and ventral to the intrapulmonary bronchus. Wolf (1933) amended Milani's model of the varanid lung to include intercameral perforations between the lung chambers (Fig. 2). He also noted that water could be passed between adjacent lateral chambers in the varanid lung and suggested that inspired air might, in a bird-like manner, flow first into the caudal sac through the intrapulmonary bronchus and then take a different path to the gas exchange regions of the lung. The distribution of gas-exchange parenchyma has been studied quantitatively (Perry, 1983), and multiple authors have made qualitative comparisons between the pulmonary anatomy of different species (Milani, 1894; Kirschfeld, 1970; Becker et al., 1989). Kirschfeld (1970) first divided the intrapulmonary bronchi into dorsal, ventrolateral, and ventromedial groups but concluded that the intercameral perforations were too small to cause appreciable air movement between secondary bronchi and may have more to do with the lightening of mechanically unnecessary septa. Becker et al. (1989) compared varanid lungs of more species than Kirschfeld, finding varying density and size of intercameral perforations between species, and concluded that the perforations have a role in airflow, but rejected Wolf's hypothesis that they provide a direct route from the saccular to the respiratory portions of the lung (Becker et al., 1989). The lungs of this species were also investigated by scanning electron microscopy of latex casts (Maina et al., 1989), which depicted the faveolar compartmentation in great detail.

Previously, our group documented unidirectional cranial flow through these perforations in the walls of some of the caudal lateral chambers using three methods: (1) measuring flow using dual thermistor flow meters in excised *Varanus exanthematicus* lungs; (2) observations of neutrally buoyant microspheres in excised, water-filled lungs; (3) using surgically implanted dual thermistor flow probes *in vivo* on awake animals breathing naturally (Schachner et al., 2013b). Much of the varanid lung, especially the region of dense parenchyma in the central and dorsal aspect of the lung, is structurally complex and made of chambers too small to investigate with these traditional methods. This study seeks to significantly expand our knowledge of the pulmonary flow pattern in this species using CFD simulations

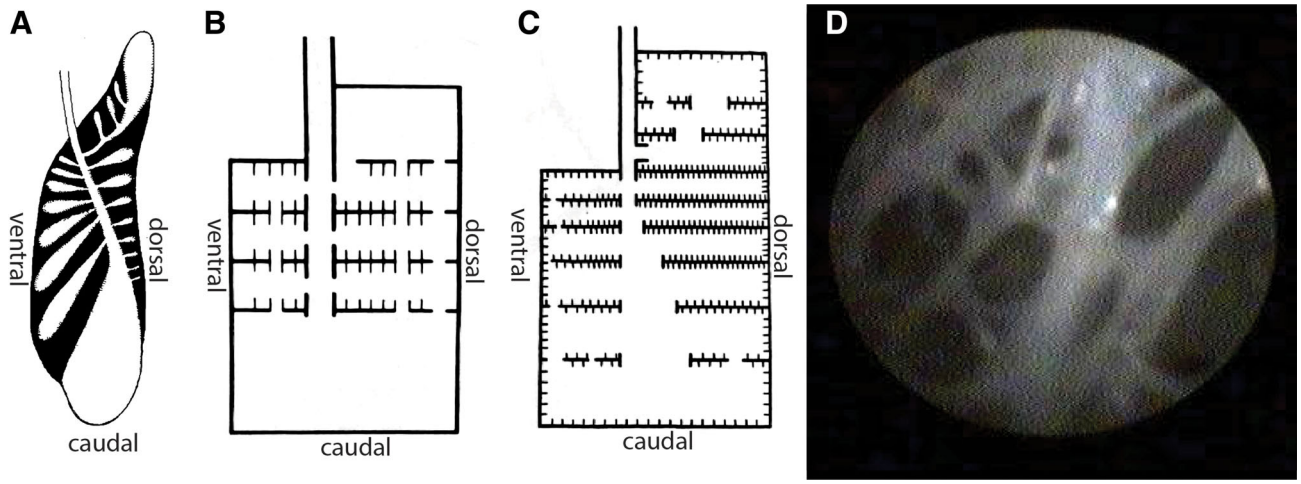

Fig. 2. Pattern of intercameral perforations. (A) Lung scheme drawn by Milani (1894) showing saccular chambers and accurate branching, but lacking perforations in the walls between secondary bronchi. (B) Illustration by Wolf (1933) showing a few connections between secondary bronchi (intercameral perforations). (C) Illustration by Kirschfeld (1970) showing a few perforations between hilar-cranial secondary bronchi and caudal bronchi. (D) Image of the wall between Chambers L9 and L8 of a 600 g *Varanus exanthematicus* taken with an endoscope, showing that some chamber "walls" are actually a filigree as they have more perforations than wall material, unlike illustrations by the previous researchers.

based on lung morphology and realistic mesh lung motion. A validated CFD model will provide insight into how air moves through all of the chambers in the varanid lung, allow multiple hypotheses regarding lung structure and flow function to be tested, and begin establishing a quantifiable framework to study pulmonary flow patterns.

MATERIALS AND METHODS

Anatomical Methods

As the basis of the CFD model, computed tomography (CT) data were collected on a live, unanaesthetized animal (680 g) at the South Jordan Health Center in Utah with a voxel size of $398.44 \times 398.44 \times 600$ μm with a current of 240 mA and 100 kV on a Siemens Somatom Definition Flash (Siemens) CT scanner. The right lung of this scan was segmented manually to study lung anatomy using Horos (The Horos Project) and Avizo (FEI Visualization Sciences, ThermoFisher Scientific) software. Lung anatomy was also assessed by segmentation of additional scans (n = 3), dissection of multiple lungs (n = 8, sex unknown, body mass 150–1,000 g), and three-dimensional (3D) printing. The 3D PDF of lung anatomy was generated with Avizo, Blender (Blender Foundation), Photoshop (Adobe Systems Inc), and Acrobat (Adobe Systems Inc.) software tools using the workflow suggested by Semple et al. (2019).

Pulmonary vascular anatomy was studied using a micro-CT of an excised varanid lung perfused with BrightVu (Scarlet Imaging). Scans were made on a Bruker SkyScanner model 1173 in the Karl Liem Imaging Facility at the Friday Harbor Laboratories, University of Washington. Scans were made at 50 kV and 150 μA with isotropic 10.1434 μm voxels. All methods were approved by the University of Utah IACUC.

CFD Simulations

Several moving-wall simulations were studied including one with an anatomically accurate mesh and three where the surface models of the segmented CT data were altered using manual segmentation tools to produce experimental meshes with the following manipulations: (1) the ostium from the intrapulmonary bronchus to the hilar-cranial bronchus was closed off, and (2) many of the walls separating the lateral and medial secondary bronchi were removed, (3) the number and size of the intercameral perforations in the lateral and medial chamber were reduced. In addition, several static, steady-state simulations were run to further investigate the role of the hilar-cranial bronchus.

The surface models were meshed into a high-fidelity computational mesh consisting of approximately 1.2 million elements using the hexahedral-dominant, unstructured mesh generation utility, snappyHexMesh, available in the open-source computational continuum mechanics library, OpenFOAM (www.openfoam.com). For the moving-wall simulations, several simulations of mesh motion alone were iterated to arrive at a tidal volume that approximated resting volume for this species based on ventilatory scaling data (Wang et al., 1997), and lung motion visually approximated from biplanar fluoroscopy recordings previously made in this species of ventilation (Cieri et al., 2018). Figure 3 shows the relative contribution of each rib to ventilation overlaid with the lung model (Cieri et al., 2018). Fluid simulations were carried out on the segregated pressure-based Pressure Implicit with Splitting of Operators (PIMPLE) (hybrid Pressure-Implicit with Splitting of Operators [PISO]/semi-implicit method for pressure-linked equations [SIMPLEs]) algorithm available in OpenFOAM to solve the time-accurate incompressible continuity and Navier–Stokes equations in an arbitrary Lagrangian–Eulerian reference frame with dynamic mesh motion and second-order accurate temporal and spatial discretization schemes. For the static models, fluid simulations were carried out in the SIMPLE algorithm. Several full breathing cycles were simulated with a breathing frequency of 15 breaths per minute with a tidal volume of 9.59 mL, and a time step of 0.0001 sec. A transient simulation of three full breathing cycles was simulated to arrive at a time-periodic steady-state solution (Fig. 4), and the second breathing cycle was analyzed.

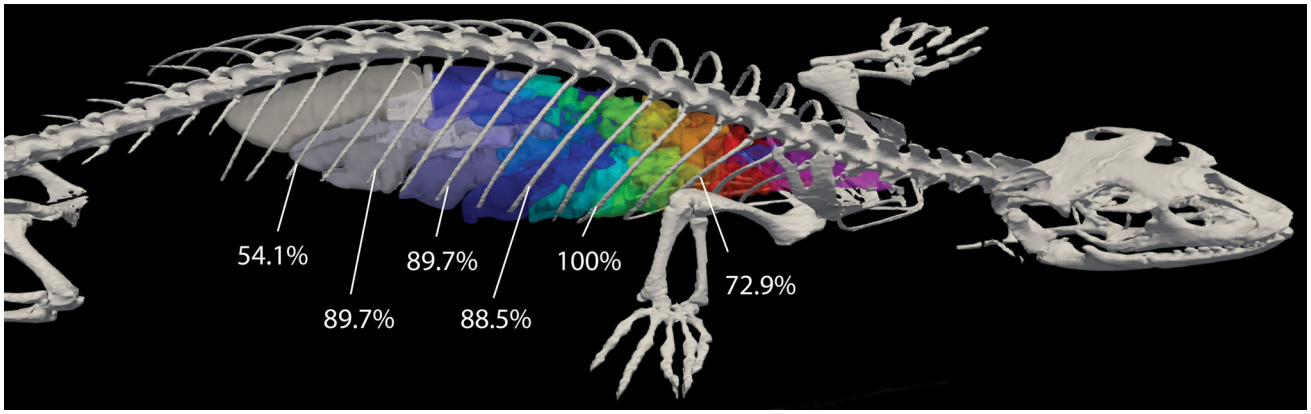

Fig. 3. Lung morphology and costal mobility during ventilation. The lung CFD model placed into anatomical position with ribs scaled by percentage to the most mobile rib as measured by with X-ray reconstruction of moving morphology analysis (Cieri et al., 2018).

OpenFOAM flow simulations were computed on four 32-core nodes at the Center for High Performance Computing at the University of Utah and on six 32-core nodes on the Blue Waters Supercomputer at the National Center for Supercomputing Applications at the University of Illinois at Urbana Champaign. The open-source visualization software ParaView (www.paraview.org) was used to visualize the flow patterns from the reconstructed numerical simulations. The ParaView slice, streamline, and glyph functions were used to visualize flow, as illustrated in Figure 5. 3D PDFs of ParaView visualizations were generated in ParaViewPlus (PDF3D, Visual Technology Services). Flux measurements were carried out in ParaView by integrating the dot product of the velocity vectors and vector normal to the relevant slice through the model and summing across one full ventilatory cycle (Fig. 5D). Flux values listed in Tables 1–5 were computed over simplified slices between secondary bronchi that do not capture the complex geometry of the connections between bronchi.

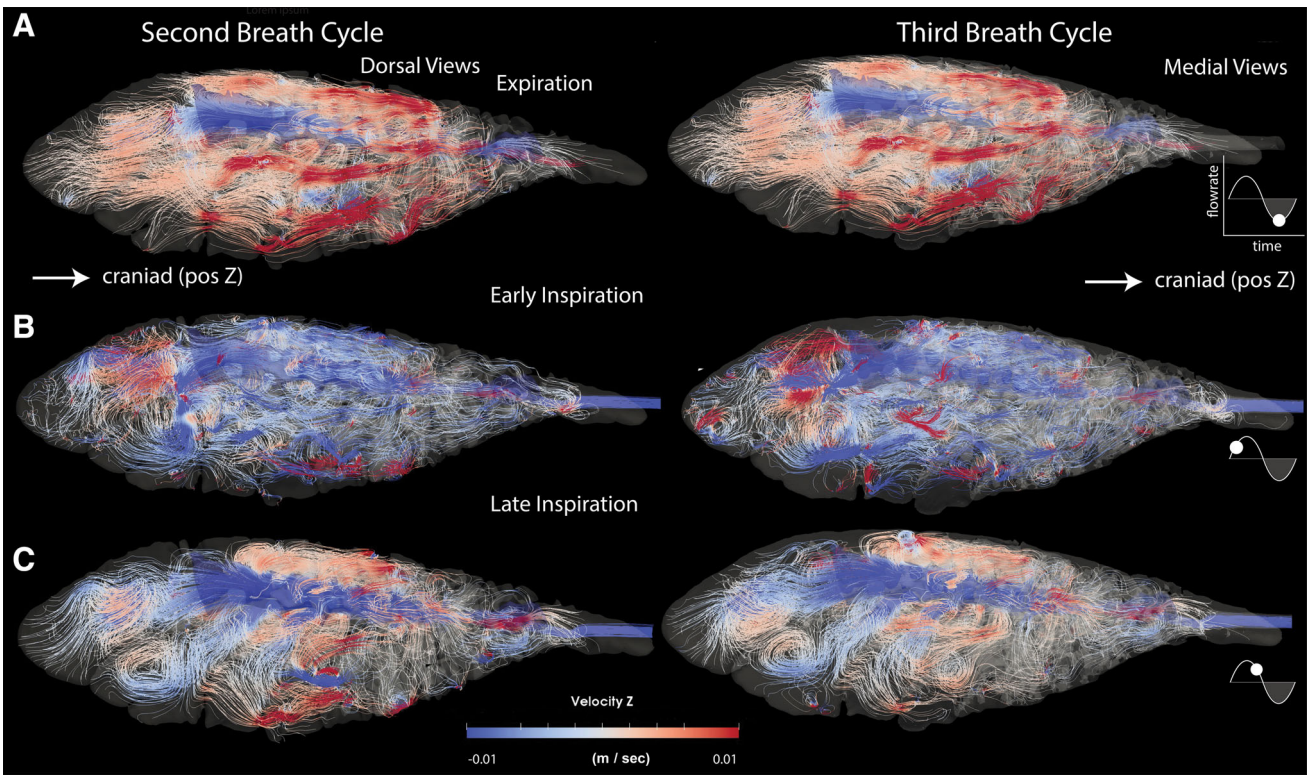

Fig. 4. Solution convergence between breaths. Streamlines from the second (left) and third (right) breath full breath cycles in the anatomically accurate (control) model are largely similar.

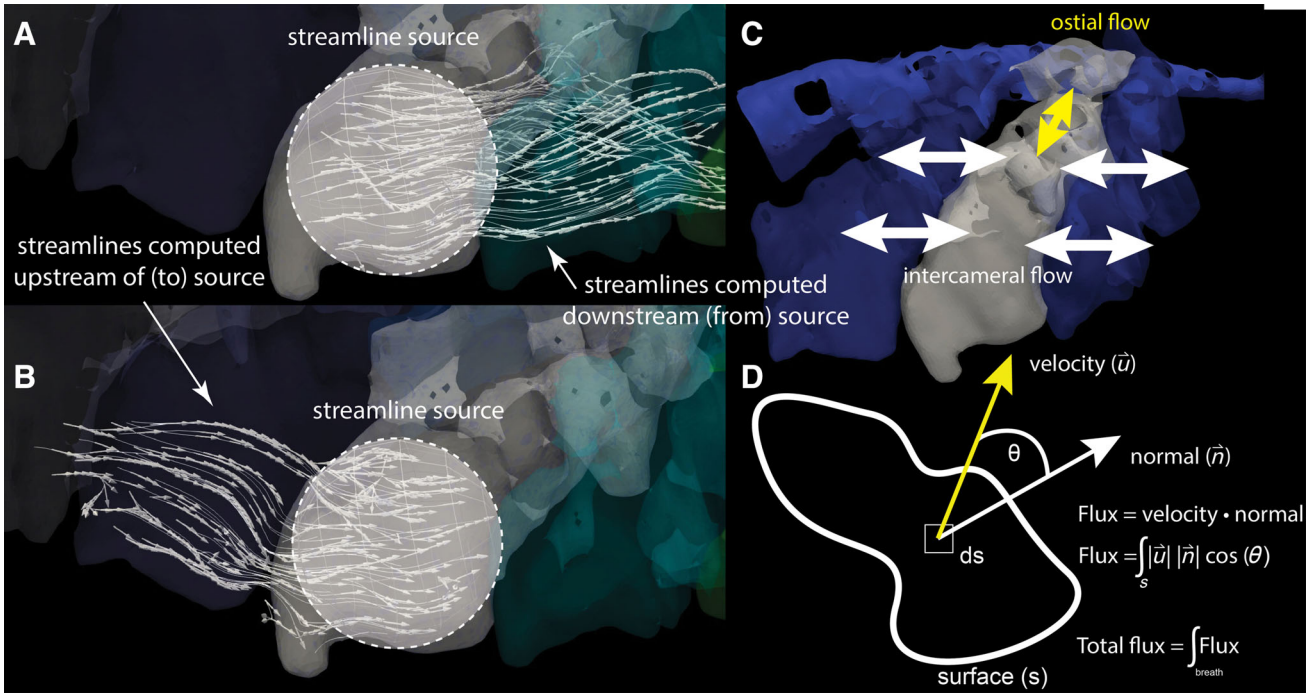

Fig. 5. Streamlines and chamber flows. CFD results are expressed as streamlines calculated upstream to (A) and downstream from (B) seed points generated within a spherical region. Arrows on the streamlines indicate local velocity vectors. (C) Flow into and out of secondary bronchi is distinguished between ostial flow—movement of air between the secondary bronchi and the intrapulmonary bronchus (yellow arrows) and intercameral flow—movement of air through the intercameral perforations between adjacent secondary bronchi (white arrows). (D) Fluxes through slices were calculated by integrating the surface integral of the dot product of surface normal vectors and velocity vectors over all time steps.

TABLE 1. Fluxes between lateral secondary bronchi in mL in the CFD model

	Caudal sac to L9	L9 to L7	L7 to L5	L5 to L4	L4 to L3	L3 and L2 to L1	L1 to hilar
Net flux during expiration[a]	3.31	6.95	4.32	6.31	8.86	5.38	2.68
Net flux during inspiration[a]	−1.14	−1.23	−0.25	−2.62	−0.96	−2.58	−1.23
Total craniad flux	4.25	8.78	5.58	7.68	10.25	5.59	2.85
Total caudad flux	2.08	3.07	1.51	3.98	2.35	2.79	1.40
Net flux[a]	2.18	5.72	4.07	3.70	7.90	2.80	1.45

See Figure 3 and the text for an explanation of the methods.
[a] Positive values are cranial.

In situ Flow Measurements

Flow patterns simulated with CFD were validated by visualizing flow in mechanically ventilated lungs using endoscopes and aerosolized lipids. The endoscope had a diameter of 0.9 mm (Model number HSF 0091000 NVK, Hawkeye Pro Microflex Boroscope, Gradient Lens Corporation) and a field of view of 55 degrees. An aerosolized lipid—Synthetic smoke (Froggy's Fog—Swamp Juice, Froggy's Fog)— was delivered into the inspired air by a fog machine (Eliminator Lighting

TABLE 2. Fluxes between medial secondary bronchi in mL in the CFD model

	Caudal sac to M6	M6 to M4	M4 to M3	M3 to M2	M2 to M1	M1 to hilar
Net flux during expiration[a]	7.17	5.63	5.44	4.18	0.43	−2.26
Net Flux during inspiration[a]	0.65	−5.93	−5.87	−4.56	−2.03	0.38
Total craniad flux	9.31	6.68	6.57	4.48	0.56	0.54
total caudad flux	1.49	6.98	6.99	4.68	2.17	2.42
Net flux[a]	7.82	−0.3	−0.43	−0.38	−1.60	−1.88

See Figure 3 and the text or an explanation of the methods.
[a] Positive values are cranial.

TABLE 3. Fluxes from the intrapulmonary bronchus into lateral bronchi and the caudal saccular chamber in mL in the CFD model

	L1	L2	L3	L4	L5	L6	L7	L8	L9	L10	Caudal sac
Net flux during expiration[a]	−2.43	−0.67	−0.20	−0.30	0.14	−0.22	−1.08	−0.01	−0.86	−0.03	2.80
Net flux during inspiration[a]	−0.91	−0.42	−0.24	−0.14	0.58	1.39	2.74	0.68	1.51	0.43	6.42
Total distal flux	0.16	0.14	0.07	0.25	1.14	1.57	2.89	0.98	2.05	0.69	9.23
Total proximal flux	3.50	1.23	0.51	0.69	0.42	0.40	1.22	0.32	1.41	0.29	0.01
Net flux[a]	−3.33	−1.09	−0.44	−0.44	0.72	1.18	1.66	0.66	0.65	0.40	9.22

See Figure 3 and the text for an explanation of the methods.
[a] Positive values indicate distal flow (out of the intrapulmonary bronchus).

TABLE 4. Fluxes from the intrapulmonary bronchus into medial bronchi and hilar bronchus in mL in the CFD model

	M1	M2	M3	M4	M5	M6	M7	Hilar
Net flux during expiration[a]	−2.97	−1.15	−0.84	−1.05	−0.34	−1.71	0.06	−4.09
Net flux during inspiration[a]	0.65	0.34	−0.08	0.70	0.63	2.49	0.73	2.39
Total distal flux	0.91	0.78	0.36	0.88	0.80	2.58	1.13	2.47
Total proximal flux	3.22	1.59	1.29	1.23	0.51	1.80	0.34	−4.16
Net flux[a]	−2.32	−0.81	−0.2	−0.35	0.29	0.78	0.79	−1.69

See Figure 3 and the text for an explanation of the methods.
[a] Positive is distal flow(out of the intrapulmonary bronchus).

Fog Machine EL-400) or an electronic cigarette. A Luxxor Video Camera System (LXX-VBSM) was used to record videos of flow at a rate of 29.97 frames per second, and the direction of airflow was determined visually.

Measurements on 3D Printed Models

The effect of airway geometry on flow patterns in the region of the hilar-cranial bronchial ostium was investigated by direct measurements on 3D printed (rapid-prototyping) models (Fig. 6). Three models were printed using 2.85 mm diameter PLA PRO material (eSun Inc) on a Raise N2 Plus Printer (Raise3D Inc) with a 0.4-mm nozzle.

The first model was made by creating a hollow tube around the actual airway geometry from the CT scan and used in the CFD model. Two additional models were modified such that either the intrapulmonary bronchus cranial to the hilar-secondary bronchial ostia was narrowed to match the diameter of the intrapulmonary bronchus just caudal to the ostium (Cranial Narrow), or such that the intrapulmonary bronchus caudal to the ostium was widened to match the diameter just cranial to the ostium (Caudal Wide) (Fig. 6B).

To determine the effect of airway geometry on the direction of flow in the hilar bronchus, measurements were initially made where one calibrated dual thermistor flow probe (Hector Engineering) with 2.5 cm of tubing on either end was held loosely inside the hilar bronchus during inspiration (Fig. 6C), where a series of constant flows ranging over physiologically realistic rates (200–2000 mL/min) were applied to the cranial end of the intrapulmonary bronchus, and expiration (Fig. 6D), where constant flow was applied to the caudal end of the intrapulmonary bronchus.

TABLE 5. Fluxes from the intrapulmonary bronchus into dorsal bronchi in mL in the CFD model

	D1	D2	D3	D4	D5	D6	D7	D8	D9
Net flux during expiration[a]	−1.12	0.38	0.41	0.47	0.23	0.04	0.61	0.18	0.24
Net flux during inspiration[a]	0.02	−0.04	−0.34	−0.82	0.11	0.02	1.71	0.79	−0.01
Total distal flux	0.45	0.77	0.76	0.68	0.48	0.43	2.37	1.05	0.43
Total proximal flux	−1.55	−0.44	−0.69	−1.13	−0.13	−0.36	−0.04	−0.08	−0.19
Net flux[a]	−1.10	0.33	0.07	−0.45	0.35	0.06	2.33	0.97	0.23
	D10	D11	D12	D13	D14	D15	D16	D17	
Net flux during expiration[a]	−0.01	0.16	0.13	0.07	−0.10	0.01	−0.01	0.00	
Net flux during inspiration[a]	−0.08	0.08	0.06	0.03	−0.24	0.40	−0.02	0.05	
Total distal flux	0.07	0.39	0.35	0.21	0.12	0.49	0.11	0.35	
Total proximal flux	−0.16	−0.15	−0.16	−0.11	−0.46	−0.08	−0.14	−0.31	
Net flux[a]	−0.09	0.24	0.19	0.09	−0.34	0.41	−0.03	0.04	

See Figure 3 and the text for an explanation of the methods.
[a] Positive is distal flow(out of the intrapulmonary bronchus).

To assess the effect of airway geometry on the relative flow rates in each branch, flow rates at the hilar bronchus and one end of the intrapulmonary bronchus were measured simultaneously with two calibrated dual-thermistor flow probes attached to the 3D print with dental impression material while constant flow (200–1,200 mL/min, corresponding to Re ~80–420 was applied at the other end of the intrapulmonary bronchus (Fig. 6E). This procedure increased the resistance by an equal amount at each downstream branch.

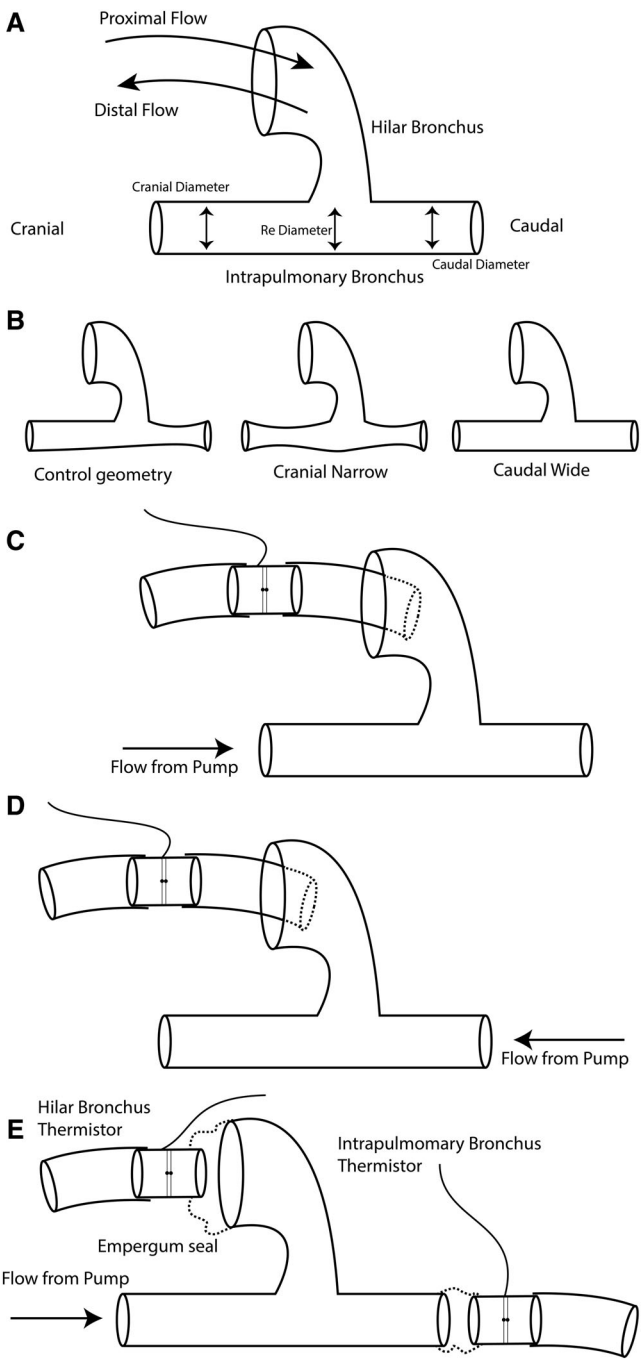

RESULTS

Anatomy

The right lung of *V. exanthematicus* consists of a central intrapulmonary bronchus (IPB) which is cartilaginous cranially with multiple ostia opening into lateral, medial, and dorsal secondary chambers (Figs. 7 and 8). The most proximal ostium on the intrapulmonary bronchus opens dorsally into a cartilaginous connection that bends cranially and opens into a wide bronchus with side chambers, called the cranial (Kirschfeld, 1970) or hilar-cranial secondary bronchus (Becker et al., 1989), hereafter the hilar-cranial bronchus (HCB) (Fig. 7A,E). The side chambers of the hilar-cranial bronchus surround the main chamber on all sides and connect through intercameral perforations with secondary bronchi that independently branch off the intrapulmonary bronchus, medially, dorsally, and laterally (Figs. 7E–H).

Caudally, the intrapulmonary bronchus features lateral, medial, and dorsal ostia along its length that open into wide secondary bronchi that connect with each other through intrapulmonary perforations of varying sizes (Fig. 7A–D). The caudal end of the intrapulmonary bronchus opens into a large, caudal, saccular chamber hereafter called the caudal sac. The intrapulmonary bronchus generally widens from cranial to caudal but narrows to 4.53 mm^2 immediately after the hilar-cranial bronchus ostium (where it has a cross-sectional area of 5.73 mm^2) (Fig. 7F). The central, dorsal aspect of the lung contains smaller chambers, more blood vessels, and more parenchyma than the ventral and distal secondary bronchi, and the hilar-cranial secondary bronchus area. The secondary bronchi not only open into the intrapulmonary bronchus but are also connected to each other through intercameral perforations (Fig. 2D).

Correspondence of Results from CFD Simulations and Visualization of Aerosolized Lipids

The pattern of flow studied by visualization of aerosolized lipids is similar to the CFD simulation in all chambers studied (Table 6), except for the caudal end of the intrapulmonary

Fig. 6. Illustration of flow measurements on 3D prints. (A) Diagram of the 3D prints showing the intrapulmonary bronchus and the proximal portion of the hilar bronchus. Locations are marked where diameters were measured proximal and distal to the hilar-bronchial ostium and at the ostium for the calculation of Reynolds numbers. (B) The three physical models printed: a control print matching the scan geometry (control print); a print where diameter was narrowed cranial to the hilar bronchus (cranial narrow), to match the diameter of the intrapulmonary bronchus distally; and a print where the distal diameter was increased to match the proximal control geometry (caudal wide). Flow measurements were made with one calibrated dual thermistor flow probe, connected to 2.5 cm of tubing on either end, was held loosely inside the hilar bronchus during inspiration (C), and a constant flow was applied to the cranial end of the intrapulmonary bronchus to simulate inspiration. Constant flow was applied to the caudal end of the intrapulmonary bronchus instead to simulate expiration (D). (E) Flow at the hilar bronchus and either end of the intrapulmonary bronchus (inspiration measurements shown) were also measured simultaneously with two calibrated dual-thermistor flow probes attached to the 3D print with dental impression material while constant flow was applied at the other end of the intrapulmonary bronchus.

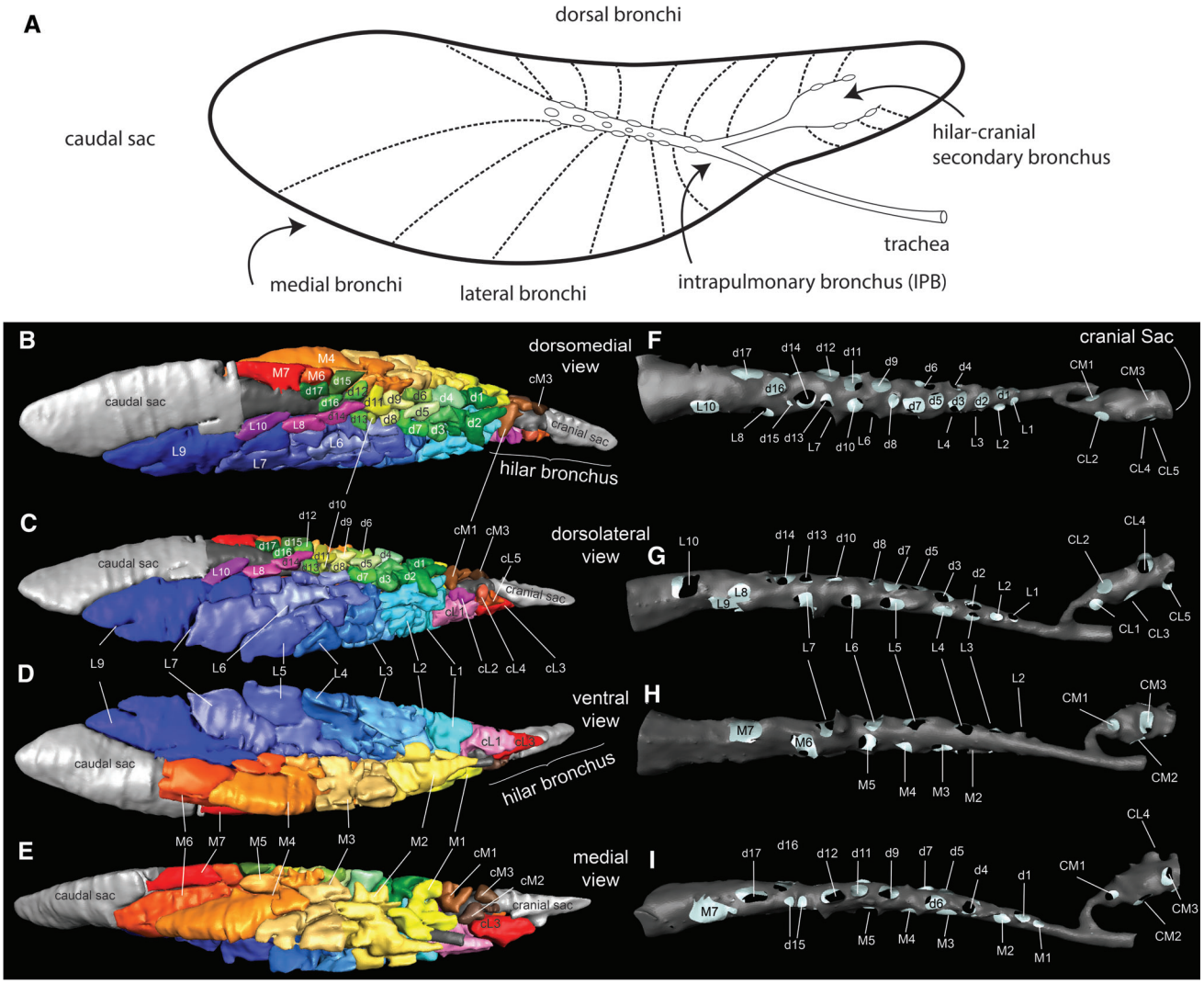

Fig. 7. Pulmonary anatomy of right lung of *Varanus exanthematicus* studied by CT. (A) Simplified line drawing in lateral view of the anatomy showing the intrapulmonary bronchus with ostia to the dorsal, lateral, and medial (not shown) bronchi, as well as the hilar bronchus. Below: Airways rendered as volumetric regions of interest (left) and the branching pattern of secondary bronchi off the intrapulmonary bronchus (right). The lung consists of an intrapulmonary bronchus which runs from the hilus to a caudal saccular chamber. The intrapulmonary bronchus branches to give rise to lateral, medial, and dorsal secondary bronchi. The first ostium off the intrapulmonary bronchus leads to the cranial aspect of the lung through a long, cartilaginous bronchus called the hilar-cranial bronchus (B) Dorsomedial view of labeled bronchi, (C) dorsolateral view of labeled bronchi, (D) ventral view of labeled bronchi, (E) medial view of labeled bronchi, (F) dorsomedial view of intrapulmonary bronchus with labeled ostia opening into secondary bronchi, (G) Dorsolateral view of intrapulmonary bronchus with labeled ostia opening into secondary bronchi, (H) ventral view of intrapulmonary bronchus with labeled ostia opening into secondary bronchi, (I) medial view of intrapulmonary bronchus with labeled ostia opening into secondary bronchi.

bronchus, which was found to be tidal in measurements on excised lungs and fully unidirectional in the CFD model. See Figure 9 and Video 1: https://players.brightcove.net/6563269 89001/default_default/index.html?videoId=6115073507001; Video 2: https://players.brightcove.net/656326989001/defau lt_default/index.html?videoId=6115074896001; Video 3: https://players.brightcove.net/656326989001/default_defau lt/index.html?videoId=6115075633001; Video 4: https://pla yers.brightcove.net/656326989001/default_default/index.ht ml?videoId=6115073199001; Video 5: https://players.brigh tcove.net/656326989001/default_default/index.html?video Id=6115072712001; Video 6: https://players.brightcove. net/656326989001/default_default/index.html?videoId=61 15073506001; Video 7: https://players.brightcove.net/6563 26989001/default_default/index.html?videoId=611507363 2001 for a comparison between patterns of flow simulated with CFD and visualized with aerosolized lipids representative bronchus. The caudal end of the intrapulmonary bronchus was tidal, however, in the model with reduced intercameral perforations (Fig. 10).

Summary of Patterns of Flow

Although simulations show both tidal and unidirectional airflow, air is generally transported caudally through the central intrapulmonary bronchus and cranially through the secondary bronchi (Figs. 11–15, Video 8: https://players. brightcove.net/656326989001/default_default/index.html?

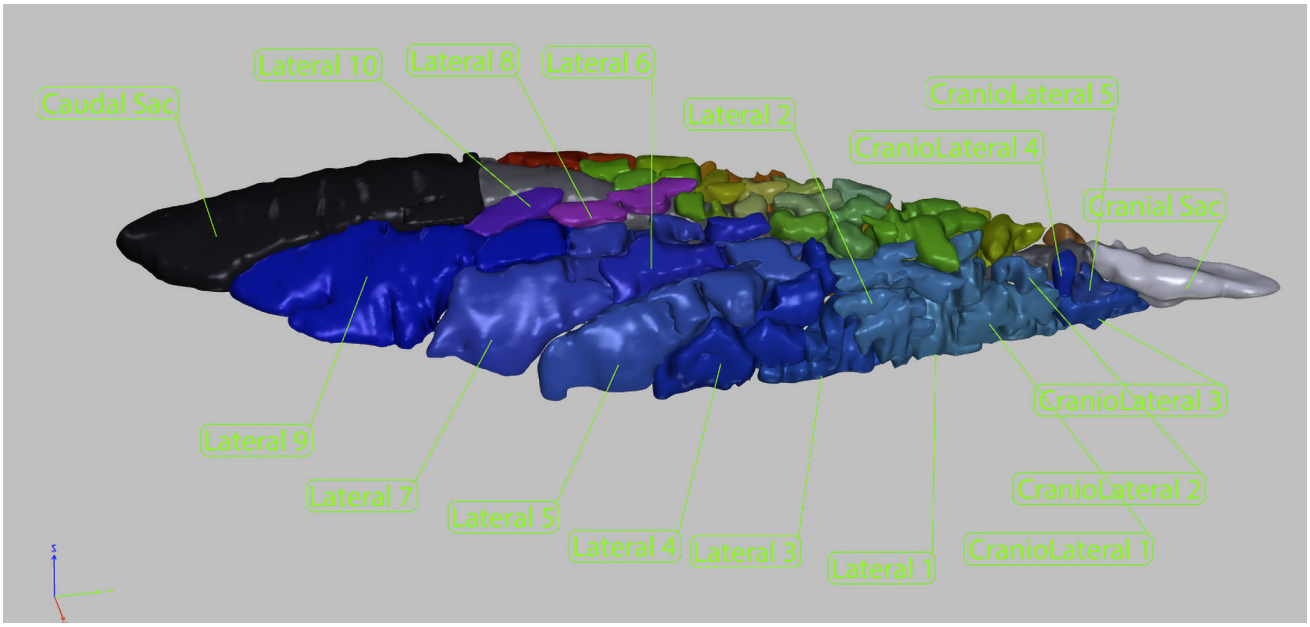

Fig. 8. Interactive 3D PDF of pulmonary anatomy of Varanus exanthematicus. Interactive content can be viewed using Adobe Acrobat. Under 3D settings (accessible with a right click onto the activated 3D PDF) reduce the framerate threshold to 4 and select "None" under "optimization scheme for low framerate" for best results. 3D PDFs in the version of record are corrupted, but can be downloaded from https://tinyurl.com/LizardLungs.

videoId=6098782189001). Relative to this overall pattern, little air flows directly between the intrapulmonary bronchus and most secondary bronchi. The simulations show that the flow direction in the secondary bronchi is largely similar during late inspiration and expiration, and opposite during early inspiration.

Inspiration. During early inspiration, air enters the lung through the trachea and flows caudally through the intrapulmonary bronchus into the caudal saclike bronchus. Some air flows into the secondary bronchi (especially the caudal secondary bronchi) and initially flows caudad between secondary bronchi. As inspiration continues, however, air switches to flow craniad within and between the secondary bronchi (Fig. 16). During inspiration, air flows into the hilar-cranial secondary bronchus from its main ostium to the intrapulmonary bronchus.

TABLE 6. Summary of smoke validation measurements

Chamber	No. of lungs
L9	2
L7	2
L5	3
L4	1
L3	1
M7	1
M4	1
Intrapulmonary bronchus	3
Hilo-cranial chamber	3
Cranial dorsal chambers	2
Middle dorsal chambers	2
Caudal dorsal chambers	2
Caudal saccular chamber	3

Expiration. During expiration, air flows cranially through the intercameral perforations between the secondary bronchi, and largely enters the intrapulmonary bronchus from the ostia located in the most proximal section of the intrapulmonary bronchi before it exits the lung via the trachea. Air also flows directly out of the hilar-cranial secondary bronchus during expiration to join the cranial flow in the intrapulmonary bronchus out of the lung.

Intrapulmonary Bronchus

According to both the CFD models and the smoke measurements, the intrapulmonary bronchus transports inspired air caudally to the secondary bronchi during inspiration (Fig. 17. In the main CFD model, airflow in the intrapulmonary bronchus switches directions during ventilation, sometimes flowing caudad, and sometimes flowing craniad, but it is unidirectional with regard to net mass transport, as much more air moves caudally through the intrapulmonary bronchus than cranially (Figs. 15 and 17). The cranial intrapulmonary bronchus is fully tidal and transports the same amount of air cranially and caudally, but the caudal intrapulmonary bronchus is net unidirectional; caudal flow rates in the caudal intrapulmonary bronchus during inspiration are much greater than cranial flow rates during expiration (Fig. 17). The ostium to the caudal sac was observed to be tidal, however, from the visualization of aerosolized lipids and in the CFD model with reduced intercameral perforations (Fig. 10).

Intrapulmonary Bronchial Ostia

With respect to the intrapulmonary bronchus, the cranial ostia are generally net incurrent (gases moving from the secondary chambers into the intrapulmonary bronchus)

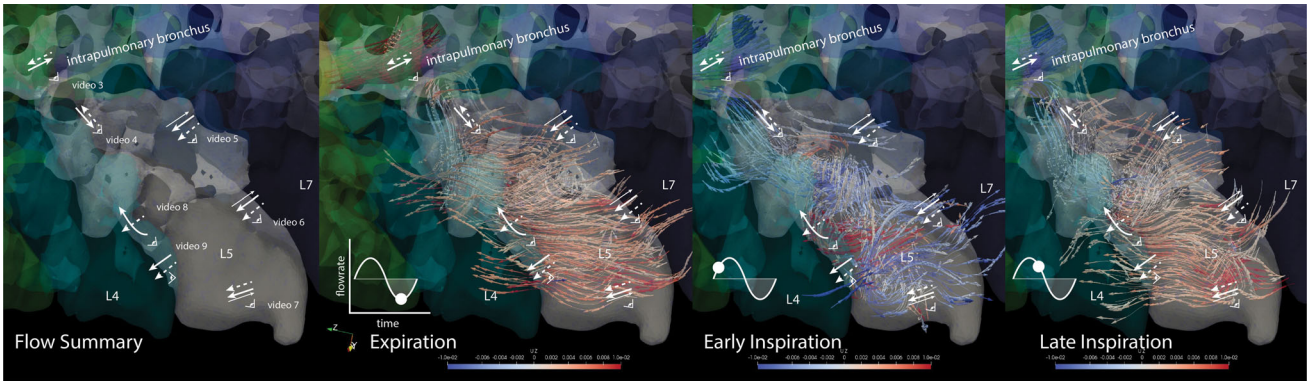

Fig. 9. Correspondence of smoke measurements and CFD simulation. Eyeballs indicate viewpoint of the endoscope. Solid white lines indicate flow direction observed from smoke visualization during inspiration, dotted lines during expiration. Video numbers correspond to smoke video locations. Colored arrows indicate local velocity vectors in the CFD model for a corresponding time step in the simulation.

channels, and the caudal ostia are net excurrent channels. That is, more air flows into than out of the intrapulmonary bronchus via the proximal ostia (Tables 1–5, Fig. 16), and more air flows out of than into the intrapulmonary bronchus via the caudal ostia. The hilar-cranial secondary bronchus also functions as an incurrent channel, as more air returns to the intrapulmonary bronchus via this chamber during expiration than leaves the intrapulmonary bronchus during inspiration. The main excurrent channel moving inspired air out of the intrapulmonary bronchus is the opening to the caudal sac. The main incurrent channel moving air back into the intrapulmonary bronchus and out of the lung is the first medial and lateral ostia. Some ostia, such as the ones to the hilar-cranial chamber are tidal but with a greater flow into the bronchus than out of it (Fig. 18), while others, such as the opening to the caudal saccular chamber, are unidirectional in the CFD model.

Secondary Bronchi

During expiration, air from the caudal saccular chamber is transported craniad into the intrapulmonary bronchus directly and through the intrapulmonary bronchus via secondary bronchi (Tables 1 and 2). The lateral secondary bronchi transport air cranially from the caudal sac to the cranial intrapulmonary bronchial ostia. The hilar-cranial secondary bronchus also serves to transport air from the cranial lateral chambers to the cranial medial chambers through the intercameral perforation in its walls.

Inspired air is temporally divided between the central, dorsal aspect of lung where the blood vessels and parenchyma are concentrated (Fig. 19A), and the distal saccular chambers (Video 9: https://players.brightcove.net/656326989001/default_default/index.html?videoId=6098782188001). During early inspiration (Fig. 19B and C), streamlines seeded in the intrapulmonary bronchus proximal to

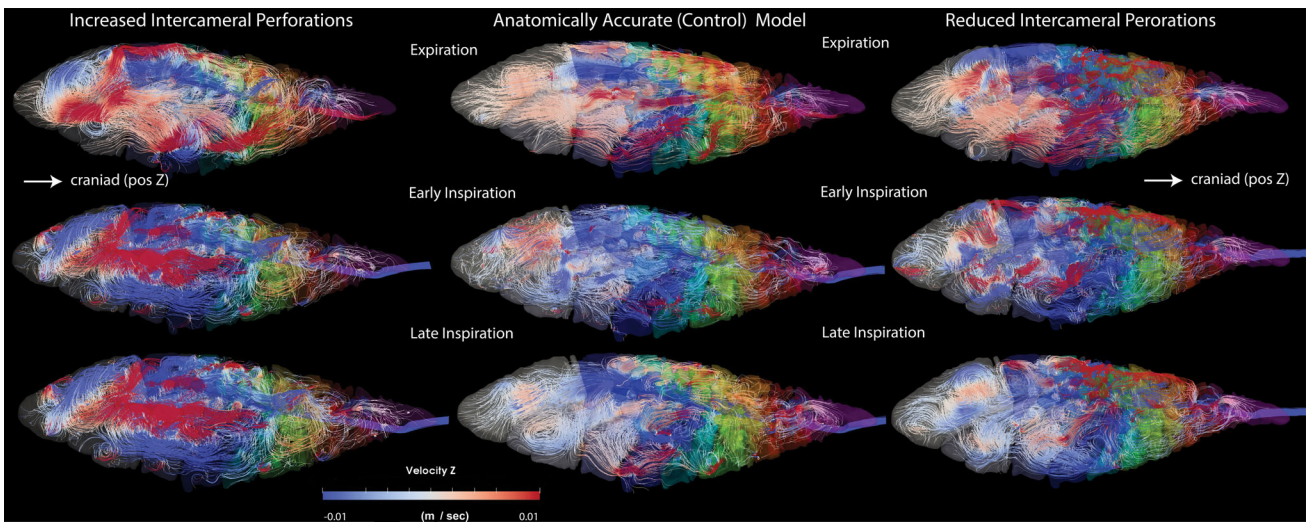

Fig. 10. Flow through CFD models with varying degrees of intercameral perforation. Streamlines showing flow direction in the original anatomically-accurate CFD model (center), in a modified model where most intercameral walls have been removed (left), and another modified model where the size and frequency of intercameral perforations was reduced (right). Streamlines are colored by the cranial-caudal component of velocity where blue indicates caudal flow and red indicates cranial flow.

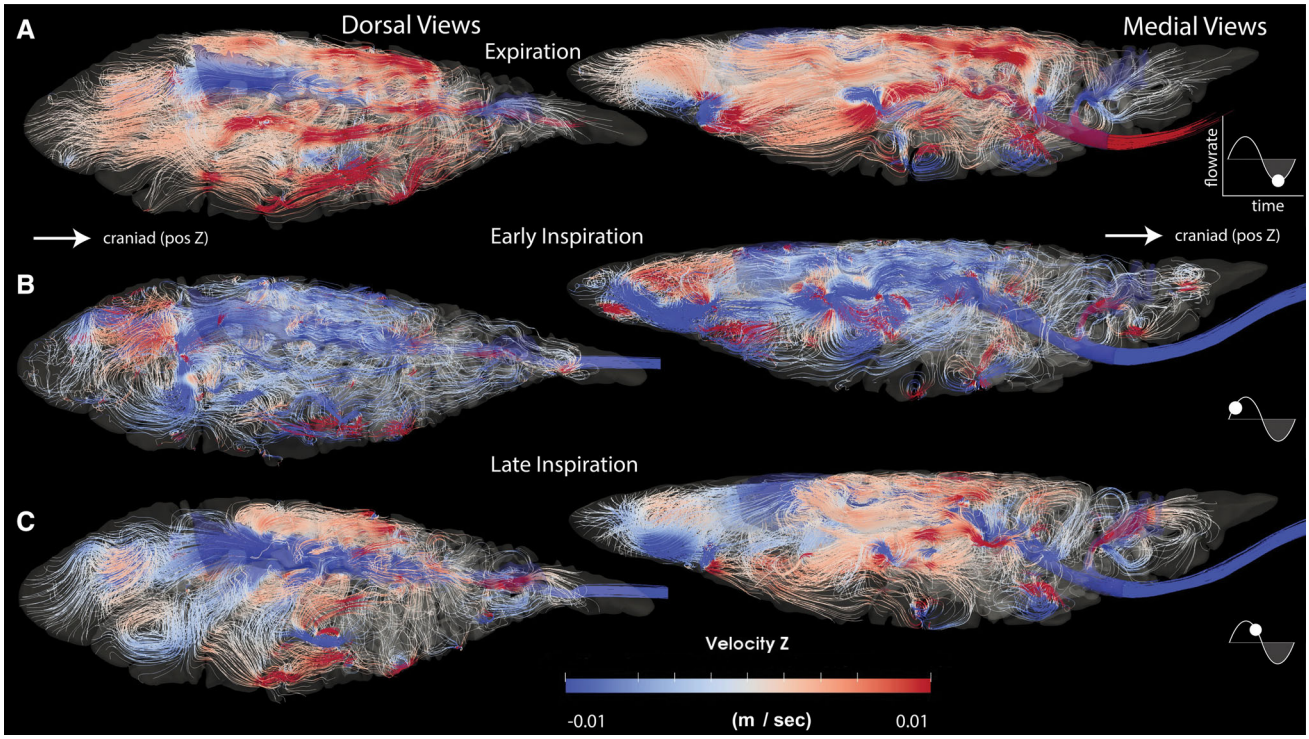

Fig. 11. Whole lung streamlines. Dorsolateral and medial views of forward and backward streamlines seeded from multiple locations in the lung model shown during mid-expiration (A), early inspiration (B), and late inspiration (C). Streamlines are colored by the cranial-caudal component of velocity where blue indicates caudal flow and red indicates cranial flow.

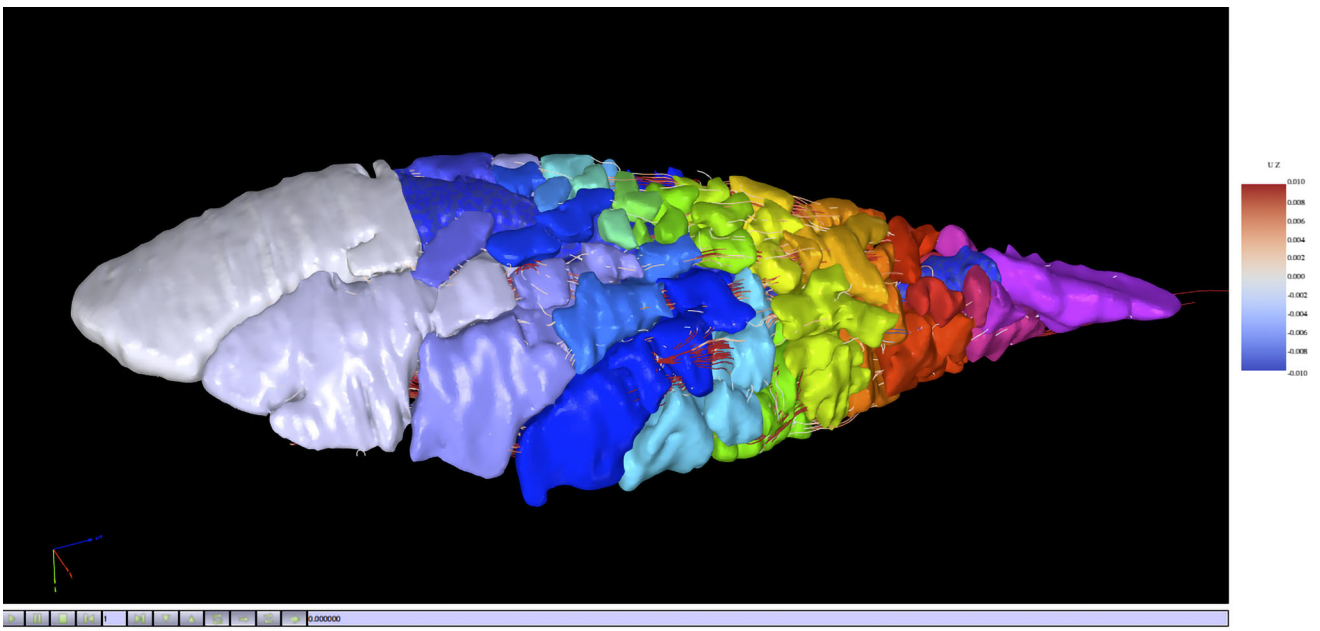

Fig. 12. Interactive 3D PDF of whole lung streamlines. Time step 1 corresponds to expiration, Time step 2 corresponds to early inspiration, and Time step 3 corresponds to late inspiration. Interactive content can be viewed using Adobe Acrobat. Under 3D settings (accessible with a right click onto the activated 3D PDF) reduce the framerate threshold to 4 and select "None" under "optimization scheme for low framerate" for best results. Flash must be installed and enabled to view animations. Interactive models for each timestep can also be viewed in 3D and virtual reality on Sketchfab https://skfb.ly/6O88r. 3D PDFs in the version of record are corrupted, but can be downloaded from https://tinyurl.com/LizardLungs.

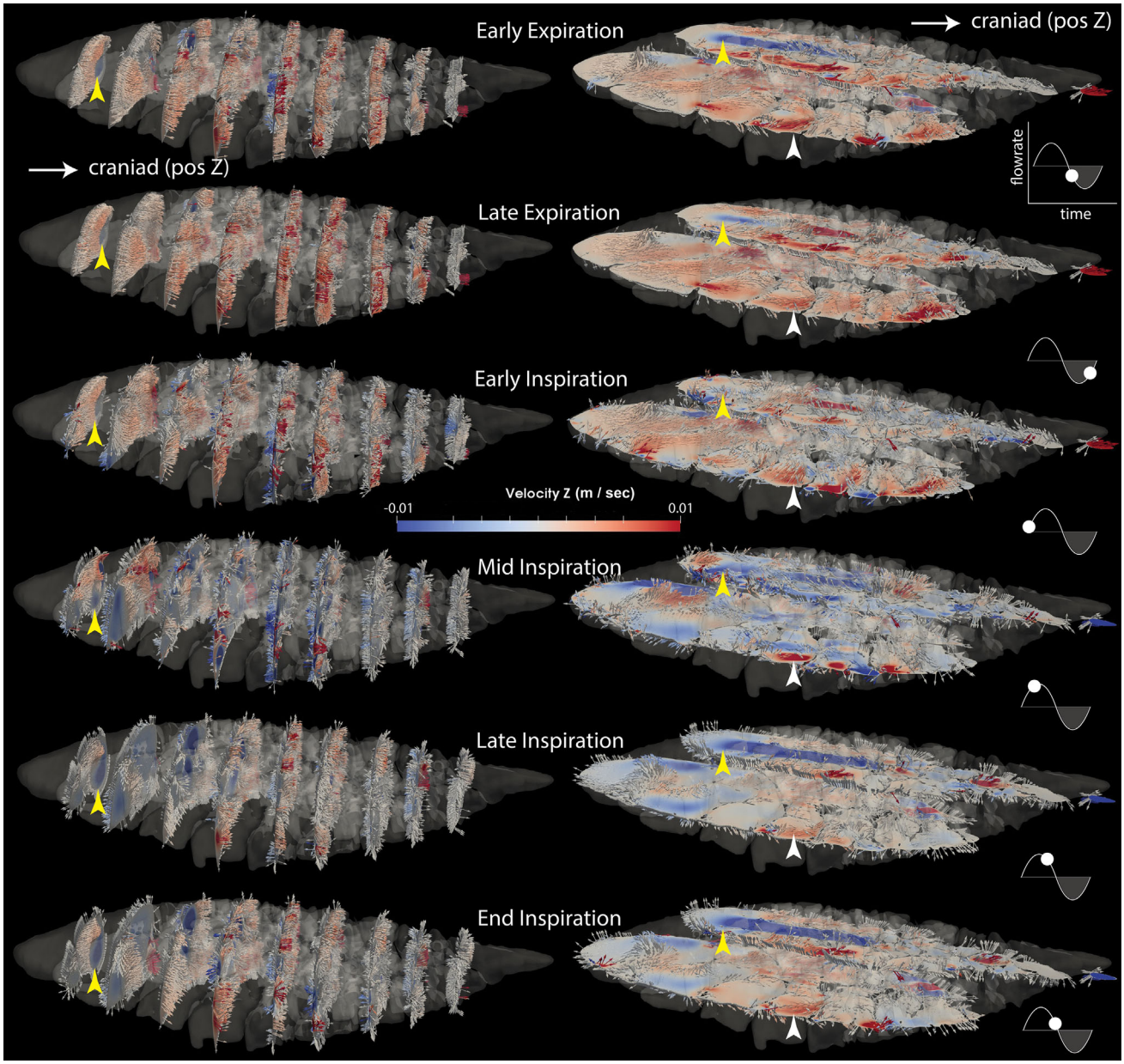

Fig. 13. Axial and coronal slices of the CFD model. Axial (left) and coronal (right) slices of the lung model shown in dorsolateral view. Arrows and slices are colored by the cranial-caudal component of velocity where blue indicates caudal and red indicates cranial flow. Yellow and white arrowheads point out some of the regions of the lung where the cranial/caudal direction of flow is consistent through most time steps.

any ostia flow downstream into the dorsal chambers through the intercameral perforations of the hilar-cranial bronchus, and their own ostia off the intrapulmonary bronchus, and through the intercameral perforations of some cranial lateral chambers. In the CFD model, during late inspiration (Fig. 19D), streamlines seeded in the same location flow downstream to the caudal sac as well as other caudal lateral and medial bronchi. A switch to craniad flow during late inspiration, however, was not observed in the smoke measurements in the caudal intrapulmonary bronchus. During expiration, air from the dorsal aspect of the lung flows through the intercameral perforations and into the hilar-cranial bronchus and then out of the lung through the hilar-cranial bronchus ostia as well as directly out of dorsal chamber ostia (Fig. 19F) and the intrapulmonary bronchus, and is replaced by air flowing from the saccular, more ventral chambers such that relatively fresh air is made to flow across the dorsal, parenchymal region of the lung during both phases of ventilation (Figs. 19E, 20, and 21).

Net flows between the walls of the secondary lateral (Table 1) or medial (Table 2) bronchi are generally higher in magnitude than through the ostia to the intrapulmonary bronchus (Fig. 22, Tables 3, 4) with the notable exception of the caudal saccular chamber, which receives almost all of its input from the intrapulmonary bronchus during both

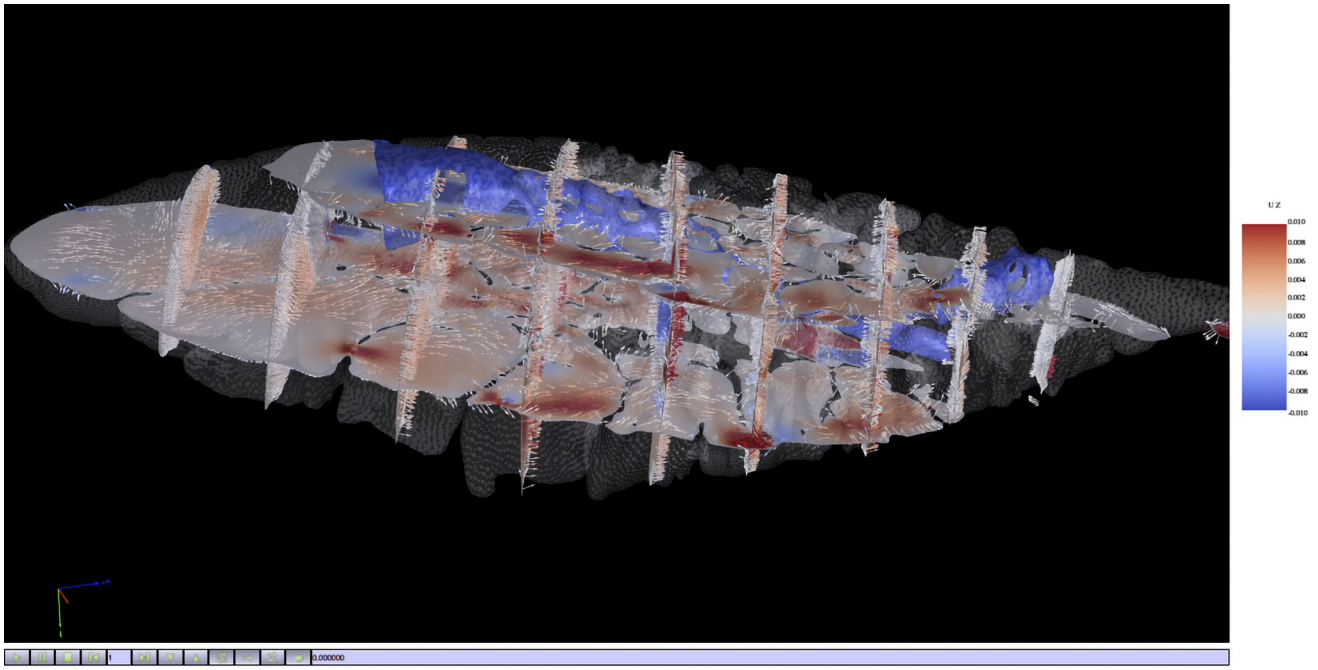

Fig. 14. Interactive 3D PDF of axial and coronal slices. Axial and coronal slices of the lung model shown in dorsolateral view. Arrows and slices are colored by the cranial-caudal component of velocity where blue indicates caudad and red indicates craniad flow. Yellow and white arrows point out regions of the lung where the cranial/caudal direction of flow is consistent through most time steps. Under 3D settings (accessible with a right click onto the activated 3D PDF) reduce the framerate threshold to 4 and select "None" under "optimization scheme for low framerate" for best results. Flash must be installed and enabled to view animations. Interactive models for each timestep can also be viewed in 3D and virtual reality on Sketchfab https://skfb.ly/6O88P.Interactive models for each timestep can also be viewed in 3D and virtual reality on Sketchfab https://skfb.ly/6O88r. 3D PDFs in the version of record are corrupted, but can be downloaded from https://tinyurl.com/LizardLungs.

inspiration and expiration. Within each bronchus, overall flow direction switches during the latter part of inspiration to match flow during expiration (Fig. 16) as ostial flow is overwhelmed by intercameral flow.

Effect of Closing off the Hilar-Cranial Bronchial Ostium

During early inspiration in the anatomically accurate model, air moves out of the intrapulmonary bronchus into the hilar-cranial bronchus to flow caudad into the medial, lateral, and dorsal secondary bronchi. During expiration, air reverses to flow into the intrapulmonary bronchus through the hilar-cranial bronchial ostium, the flow coming through the intercameral perforations in the walls from medial, lateral, and dorsal secondary bronchi.

In a CFD model where the ostium between the intrapulmonary bronchus and the hilar-cranial secondary bronchi is closed off, air spins around in the hilar-cranial

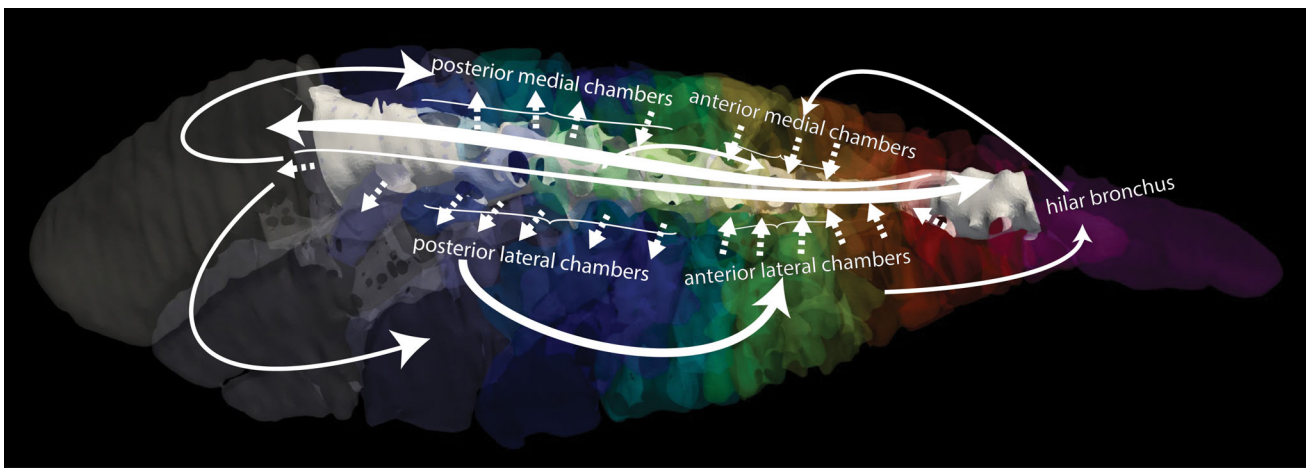

Fig. 15. Lung flow scheme in *Varanus exanthematicus*. Arrows show the overall lung scheme as studied by CFD and direct methods. White lines show overall flow direction and dotted lines indicate net ostial flow directions. Note the bird like pattern where the distal ostia have net flow from the intrapulmonary bronchus into the chambers whereas the proximal ostia have net flow from the chambers into the intrapulmonary bronchus.

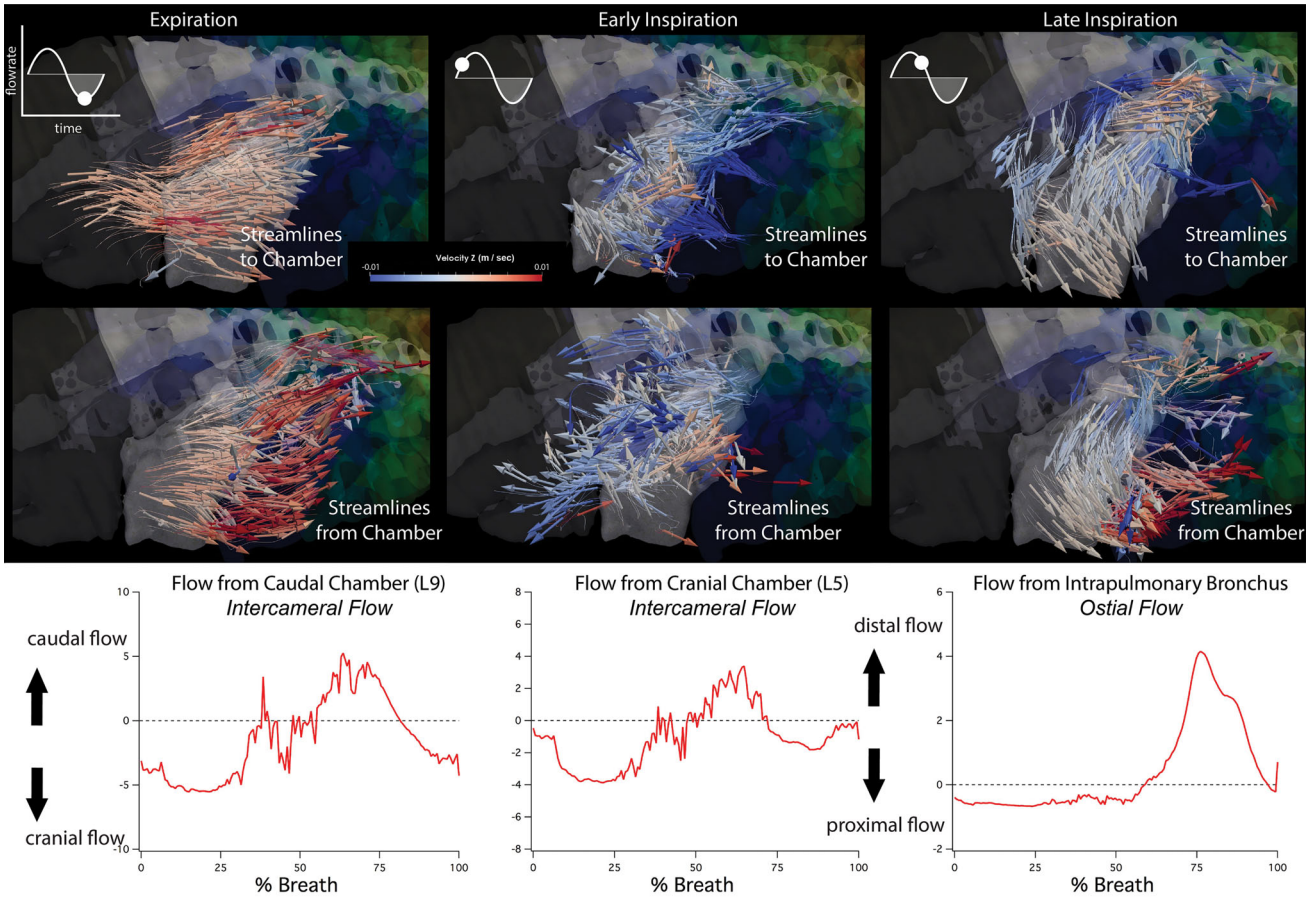

Fig. 16. Flow into and out of a representative lateral bronchus. Streamlines in lateral Chamber 7 with velocity arrows (above) colored by cranial to caudal direction where blue is caudal and red is cranial flow. Below, flow rate between the chamber and the next most caudal chamber (left), next most cranial chamber (middle) and between Chamber 7 and the intrapulmonary bronchus (right).

bronchus during inspiration and flows caudad toward the medial chambers from the hilar-cranial bronchus during expiration (Fig. 23). Without an open hilar-cranial bronchial ostium, the simulation also shows reduced cranial intercameral flow during expiration and reduced caudal intercameral flow during inspiration among the cranial secondary bronchi as well as increased recirculation during inspiration in the caudal secondary bronchi.

Effect of Removing the Intercameral Walls

In a model where most of the intercameral walls between lateral and medial secondary bronchi were removed, the pattern of flow is qualitatively different from that of the anatomically accurate model (Fig. 10). During expiration, when the intercameral walls are removed, air flows from some of the craniodorsal chambers back into the intrapulmonary bronchus and adjacent lateral chambers instead of flowing craniad. In addition, air flows caudally along the medial aspect of the caudal saccular chamber, and from the intrapulmonary bronchus through ostia into medial and lateral secondary bronchi, instead of flowing mainly craniad. Also when the intercameral walls are removed, the magnitude of airflow in the lateral chambers is increased compared to the anatomically accurate model.

Effect of Reducing the Intercameral Perforations

In the model where the size and frequency of the intercameral perforations between lateral and medial chambers are reduced, less cranial flow is observed during inspiration through the lateral and medial secondary bronchi, but more cranial flow is observed during inspiration through the dorsal secondary bronchi (Fig. 10). Also in this model, less caudal flow is observed in the caudal aspect of the intrapulmonary bronchus during inspiration, and the flow pattern in this region is overall tidal.

Flow Through 3D Printed Models

When constant flows between 250 and 2000 mL/min (corresponding to Reynolds numbers ~80–7,020) were applied to one end of the intrapulmonary bronchus with the other one left open to atmosphere (Fig. 6C,D), air was found to flow distad through the hilar bronchus in all geometries tested during inspiration (Table 7). During expiration, air was found to always flow distad through all flow rates through the “Cranial Narrow” and “Caudal Wide” prints. Air flowed proximad through the hilar bronchus in the control geometry print when the flow rate was above 300 mL/min.

TABLE 7. Flow direction in hilar bronchus when constant flow is applied (see Figure 5) to one of the intrapulmonary bronchus (cranial end during simulated inspiration and caudal end during simulated exhalation) of the 3D prints and flow direction is measured with a dual thermistor flow probe held lightly to the opening to the hilar bronchus

Pump flow rate	Model geometry	Flow conditions	Hilar flow direction
250	Control	Inspiration	Distal
		Expiration	No flow
	Downstream widened	Inspiration	Distal
		Expiration	Distal
	Upstream narrowed	Inspiration	Distal
400	Control	Inspiration	Distal
		Expiration	Proximal
	Downstream widened	Inspiration	Distal
		Expiration	Distal
	Upstream narrowed	Inspiration	Distal
600	Control	Inspiration	Distal
		Expiration	Proximal
	Downstream widened	Inspiration	Distal
		Expiration	Distal
	Upstream narrowed	Inspiration	Distal
		Expiration	Distal
1000	Control	Inspiration	Distal
		Expiration	Proximal
	Downstream widened	Inspiration	Distal
		Expiration	Distal
	Upstream narrowed	Inspiration	Distal
2000	Control	Inspiration	Distal
		Expiration	Proximal
	Downstream widened	Inspiration	Distal
		Expiration	Distal
	Upstream narrowed	Inspiration	Distal

When constant flows between 250 and 1,200 mL/min (corresponding to Reynolds number range ~80–420) were applied to the 3D prints with dual thermistor flow probes sealed to both branches (Fig. 6E), more air flowed through the intrapulmonary bronchus than the hilar-cranial bronchus during both phases of simulated ventilation (Fig. 24). During simulated inspiration, the proportion of flow that went into the hilar-cranial branch increased as flow increased in the control geometry print but remained consistent with upstream flow in the other prints. During simulated expiration, the proportion of hilar flow increased with flow rate in all three prints but increased most strongly in the "Caudal Wide" print.

Flow Through Static CFD Models

When ventilation was simulated with static, steady-state models (Fig. 25E), more cranial flow in the hilar-cranial bronchus occurred during inspiration when air was permitted to flow through the hilar-cranial bronchus boundary patch (Fig. 25C) than when the patch was closed off (Fig. 25A). During expiration, more caudad flow in the hilar-cranial bronchus occurred when positive pressure was applied at the hilar-cranial boundary patch (Fig. 25D) than when the patch was closed off (Fig. 25B). When expiration was simulated with the hilar-cranial bronchus patch set to zero pressure, air flowed cranially through the hilar-cranial secondary bronchus (Fig. 25F).

In the secondary bronchi caudal to the hilar-cranial bronchus, increased craniad flow during inspiration occurred when the hilar-cranial bronchus was opened to the atmosphere, causing the middle part of the lung to be more unidirectional under this condition (Fig. 25).

DISCUSSION

The main findings of this investigation are that the pattern of flow in the lung of *V. exanthematicus* is net unidirectional, where many lung chambers move air preferentially in one direction during the ventilatory cycle, and some intrapulmonary bronchial ostia are net incurrent and others are net excurrent channels. These results complement the results of a previous study from our group (Schachner et al., 2013b) by expanding on it and detailing similarities and differences with patterns of flow in archosaurs. Air flows primarily caudad through the distal portion of the intrapulmonary bronchus and craniad through intercameral perforations in the walls of the lateral, medial, and dorsal bronchi. The filigree that separates the chambers allows the passage of air through a route other than the intrapulmonary bronchus, and thus has a function for airflow that is similar to the parabronchi of birds. Like birds, most of the proximal (cranial) ostia carry gases from the secondary bronchi (lung chambers) into the intrapulmonary bronchus and most of the distal (caudal) ostia carry gases from the intrapulmonary bronchus into secondary bronchi. The net unidirectional flow throughout the lung arises from the collective action of multiple unidirectional bronchi, where the direction of flow often reverses during the ventilatory cycle, such that early inspiratory flow is in a different direction from late inspiratory flow and expiratory flow. Reversal in the direction of flow that is heterogenous spatially at different phases during the ventilatory cycle has also been simulated and observed in physical models of the trachea and primary bronchi of mammalian airways during high-frequency ventilation (Heraty et al., 2008). We can detect

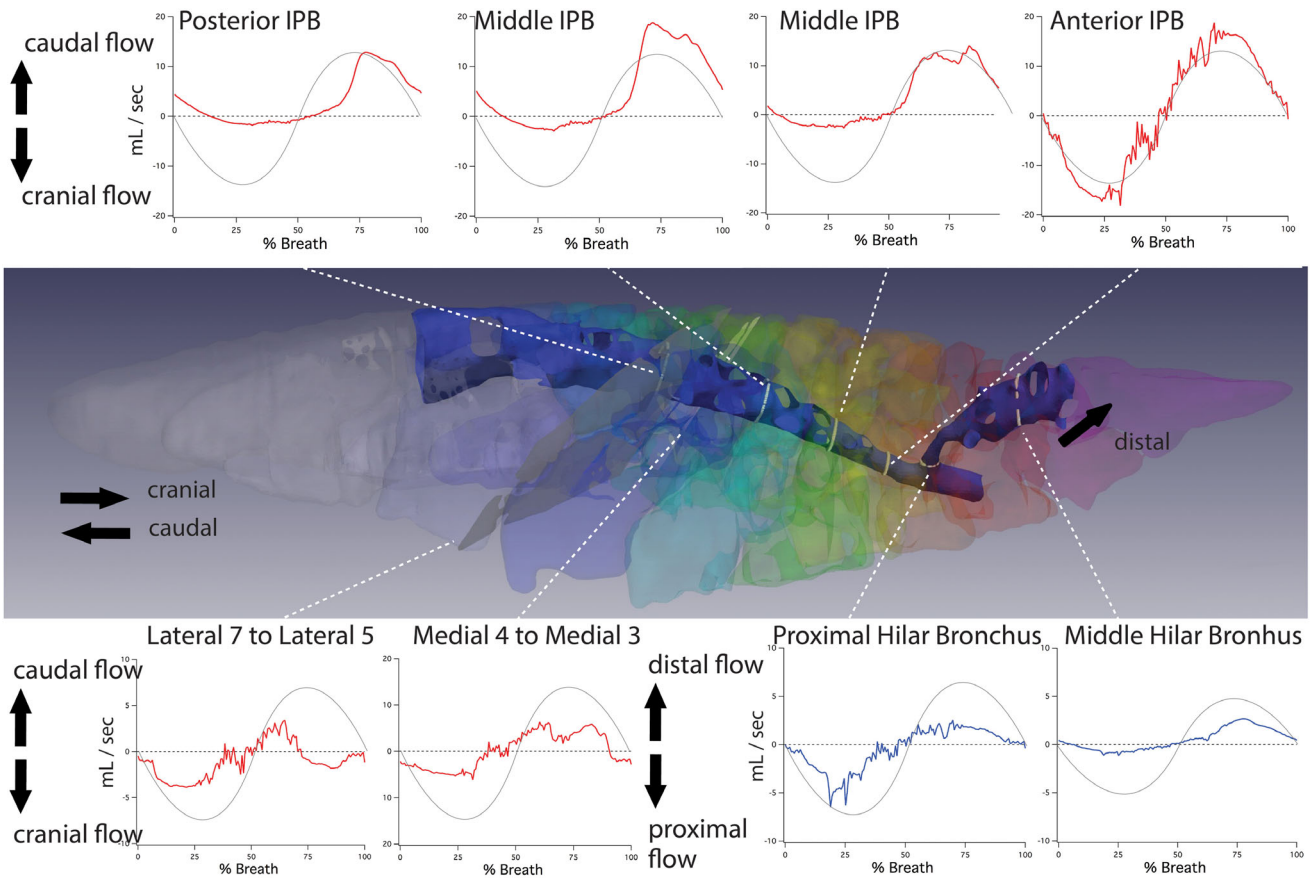

Fig. 17. Intercameral and intrapulmonary bronchus flow rates. Flow rates through the CFD model during the ventilatory cycle shown for multiple sections of the intrapulmonary bronchus (top) and between successive lateral and medial chambers (bottom left) and the hilar-cranial bronchus (bottom right). Gray traces overlaid on graphs show what flow rates may look like if lung airflow was perfectly tidal.

these flow reversals due to our ability to visualize and simulate flow, both improvements over the previous measurement techniques used in Schachner et al. (2013b).

Although the mechanisms governing the pattern of pulmonary airflow in *V. exanthematicus* are complex and remain poorly understood, our results suggest that convective inertia, and the relative resistance between the intrapulmonary bronchus vs. between adjacent secondary bronchi via the intercameral perforations are an important determinant of the flow pattern. During inspiration, a strong jet of air moves caudally through the intrapulmonary bronchus, into the lateral and medial chambers, and into the caudal saccular chamber. In the control model and the increased intercameral perforation model, this caudal jet persists into expiration, presumably because the jet's inertia is sufficient to overcome the resistance of the second pathway between the secondary bronchi. Iguana lungs work similarly, where the inspired jet of caudad-flowing air along the lateral edge which causes air to flow craniad along the medial walls (Cieri et al., 2014). In the reduced intercameral perforation model and the flow observations on real lungs, the inspiratory caudal jet reverses direction during expiration, presumably because the inertia of the inspired jet is not sufficient to overcome the increased resistance of the second pathway between the secondary bronchi is sufficiently high. Because the direct flow observations largely corroborate the flow pattern of the control model except in the caudal intrapulmonary bronchus, the real degree of intercameral perforation is probably intermediate between the control model and the reduced intercameral perforation model. Future studies that incorporate more species of varanids, which are known to vary in the distribution of intercameral perforations (Becker et al., 1989), would help to determine how these structures affect pulmonary airflow patterns.

The caudo-cranial taper in the intrapulmonary bronchus may also help to make the secondary path through the intercameral perforations the favorable path for flow. Strong caudal flow in the cranial intrapulmonary bronchus may also act to entrain flow out of the ostia opening into secondary bronchi via the Bernoulli effect, causing craniad flow to develop during inspiration and then continue during expiration due to its own inertia. This mechanism may explain why the intrapulmonary bronchus narrows after the hilar-cranial bronchus branches off (see more below) and would be similar to inspiratory aerodynamic valving in birds except that inspired air entrains flow out of the ostia instead of just bypassing it.

Interestingly, the hilar-cranial secondary bronchus, though a net inlet into the intrapulmonary bronchus, differs from the most proximal secondary bronchus of birds and crocodilians by containing tidal flow, albeit the volume of air that flows through this inlet is greater on

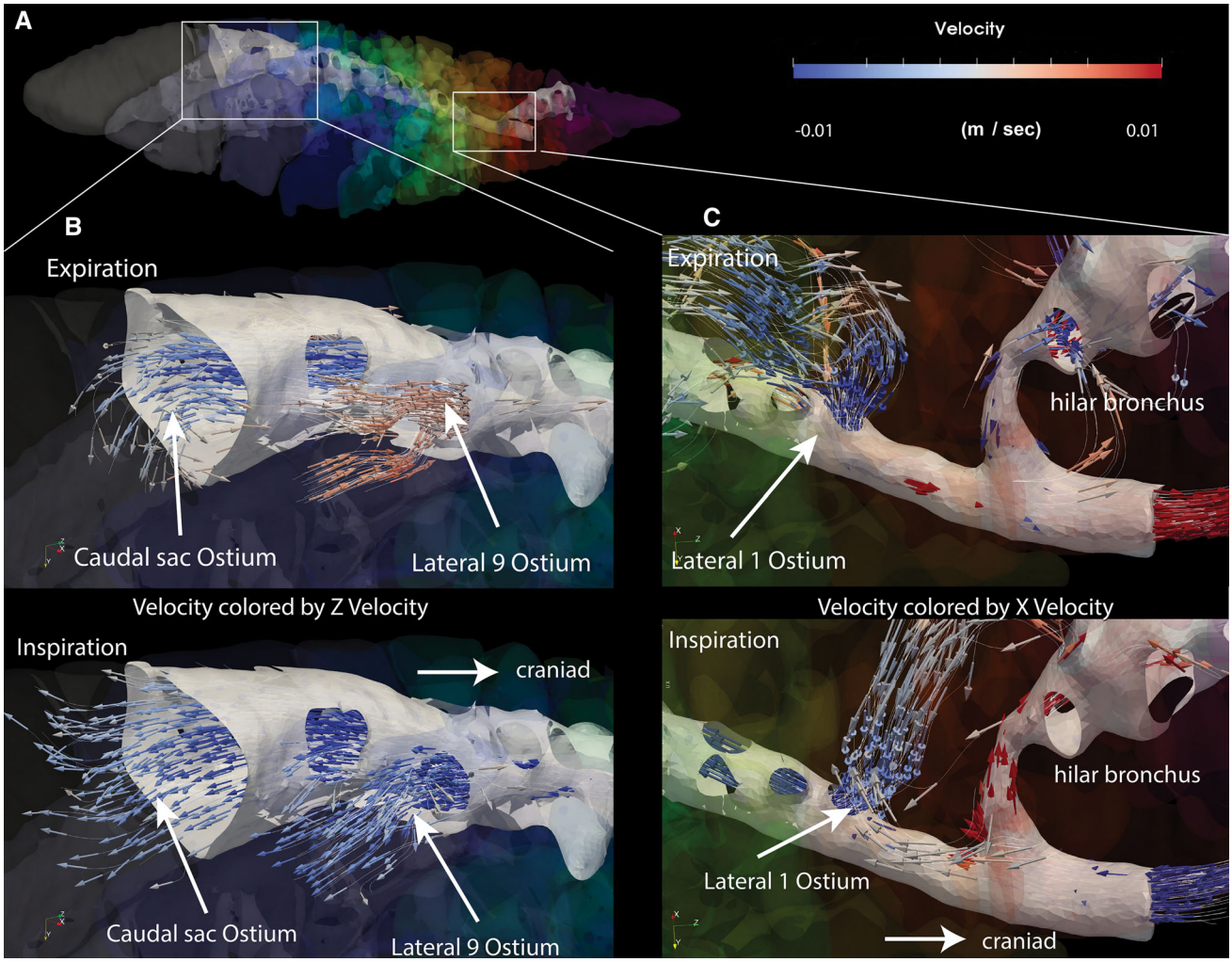

Fig. 18. Unidirectional and tidal ostia from the intrapulmonary bronchus to secondary bronchi. (A) Diagram of entire CFD model showing enlarged regions. (B) Arrows showing flow direction through the ostium to the caudal sac and Lateral 9 chamber during expiration (top) and inspiration (bottom). (C) Arrows showing flow direction through the ostium to the hilar-cranial bronchus and the Lateral 1 chamber during expiration (top) and inspiration (bottom).

exhalation than on inhalation. Tidal flow in the hilar-cranial bronchus may play a role in ventilating the capillary-dense parenchyma that lies dorsally and centrally in the lung and may be especially important when the animals are using gular pumping during exercise, rather than relying on costal inspiration. During inspiration, some presumably fresh inspired air travels from the intrapulmonary bronchus to the dorsal chambers via the hilar-cranial bronchus. This pathway may become more important during small breaths, such as gular pumps (Owerkowicz et al., 1999) where there is not sufficient tidal volume to ventilate the dorsal chambers through their main ostia. This hypothesis should be considered in future investigations. Furthermore, the transport of fresh air to the dorsal chambers via the hilar-cranial bronchus is disrupted in the CFD model when the ostium to the hilar-cranial bronchus from the intrapulmonary bronchus is occluded. In the control simulation, air flows from the hilar-cranial bronchus to the dorsal and medial chambers during inspiration, but in the simulation where the hilar-cranial bronchus ostium is ablated; however, air flows from the hilar-cranial bronchus to the dorsal and medial chambers only during expiration. Finally, increased tidal flow in the hilar-cranial bronchus in static simulations caused the flow in the secondary bronchi immediately caudal to the hilar-cranial bronchus to be more unidirectional, further suggesting that tidal flow in the hilar-cranial bronchus is important for rectifying lung flow in varanids. If this hypothesis is true, the hilar-cranial bronchus should be a consistent feature of different varanid species.

Tidal flow in the hilar-cranial bronchus also raises questions about the evolution of inspiratory aerodynamic valving in general. In alligators (Farmer and Sanders, 2010) and crocodiles (Farmer, 2015b), the first opening off the primary bronchus is termed the cervical ventral bronchus, and airflow is always caudad. In birds, the first ostia of the intrapulmonary bronchus are ventrobronchi, which are believed to always carry flow back into the intrapulmonary bronchus from the parabronchi (Maina, 2006). In both taxa, inspired air is thought to bypass the

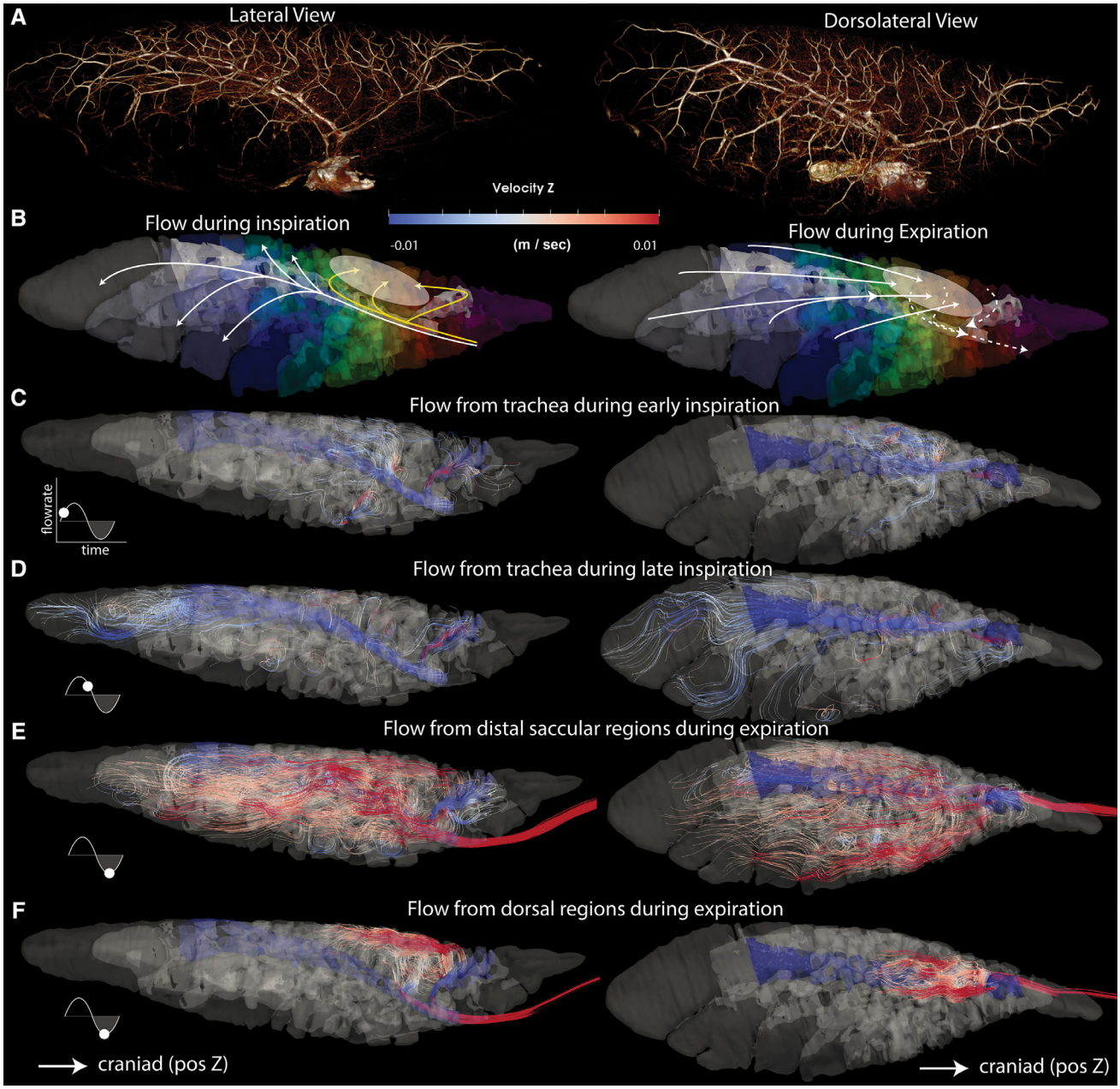

Fig. 19. Lung airflow pattern in relation to gas-exchanging parenchyma. (A) The anatomy of the pulmonary vasculature shown by CT in lateral (left) and dorsolateral (right) views. (B) Diagram showing flow patterns toward and away from the dorsal concentration of gas-exchanging parenchyma during inspiration (left) and expiration (right). Left: Yellow arrows depict inspiratory flow reaching the dorsal concentration during early inspiration and white arrows depict flow reaching the caudal, saccular chambers later in inspiration. Right: Solid arrows depict expiratory flow from the saccular chambers to the dorsal concentration and dashed arrows depict expiratory flow from the dorsal concentration out of the lung. (C) Streamlines seeded in the trachea showing downstream flow during early inspiration. (D) Streamlines seeded in the trachea showing downstream flow during late inspiration. (E) Streamlines seeded in the saccular chambers showing downstream flow during expiration. (F) Streamlines seeded in the dorsal concentration showing downstream flow during expiration. Streamlines are colored by the cranial-caudal component of velocity where blue indicates caudal flow and red indicates cranial flow.

proximal or early cranial ostia, a phenomenon termed inspiratory aerodynamic valving. The inspiratory aerodynamic valve is hypothesized to function via convective inertia ($\rho\mu^2$—gas density times velocity squared) such that the inspired air has enough momentum to avoid turning a corner (Butler et al., 1988). Previous work investigating inspiratory valving in physical models of the bird lung (Wang et al., 1988) found that the efficacy of the inspiratory valve depended on gas density and velocity (consistent with the convective inertia hypothesis) and the geometry upstream to the bifurcation, but not with the geometry or branching angle of the bifurcation. In

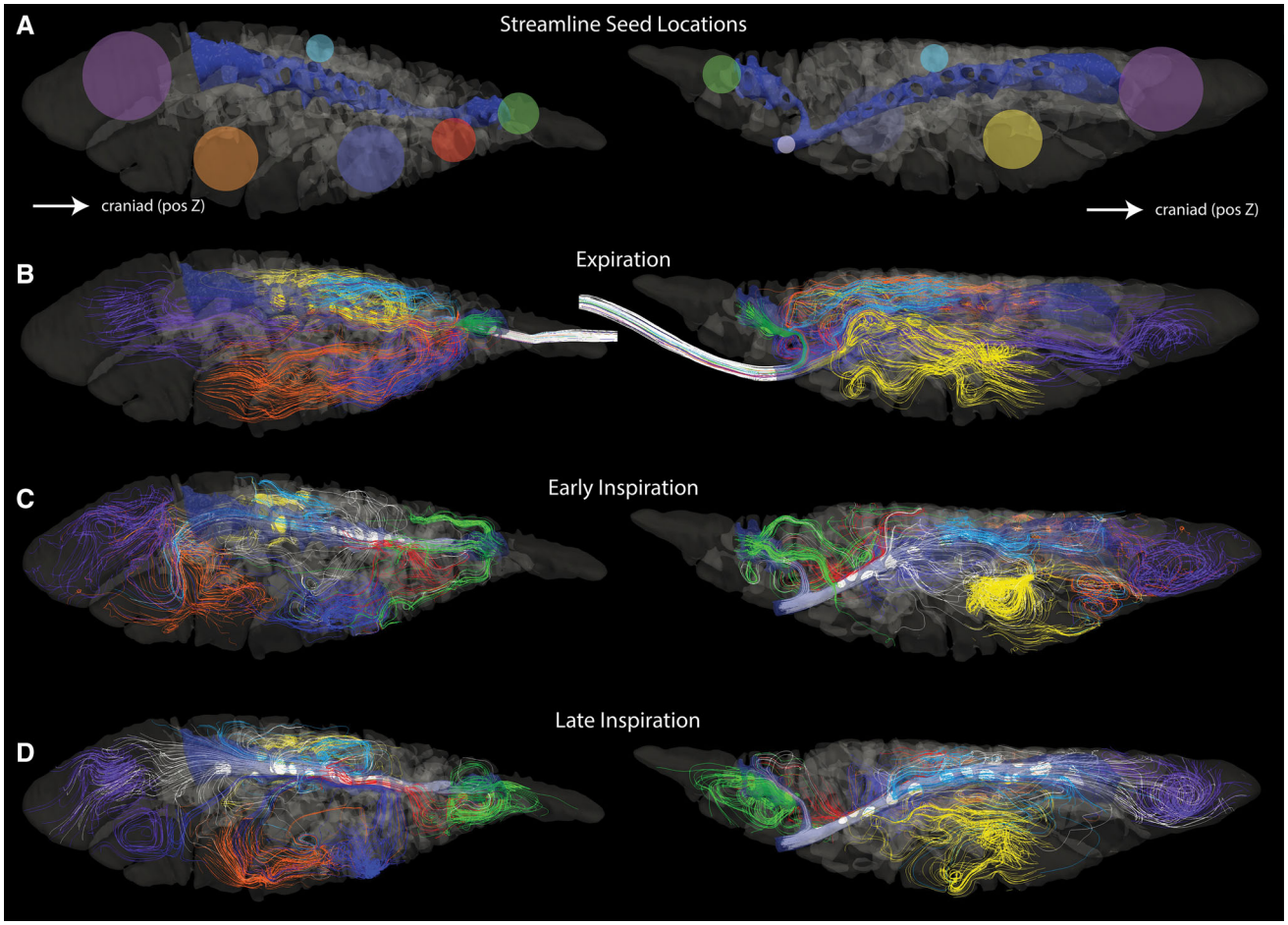

Fig. 20. Regional streamlines showing intercameral flow. Dorsolateral (left) and dorsomedial (right) views of forward streamlines seeded from multiple locations in the lung model shown during mid-expiration (A), early inspiration (B), and late inspiration (C), and colored by seed location. White streamlines were seeded in the intrapulmonary bronchus proximal to the first side bronchus (the hilar-cranial bronchus), green streamlines were seeded in the main lumen of the hilar-cranial bronchus, red streamlines were seeded in the central lumen of L1, orange streamlines were seeded in the central lumen of L8, purple streamlines were seeded in the main lumen of the caudal saccular bronchus, yellow streamlines were seeded in M4, dark blue streamlines were seeded in L3 and L4, and turquoise streamlines were seeded in D9–D11.

their models, decreasing the diameter of the airways proximal to the bifurcation caused the inspired air to accelerate, increasing its convective inertia, such that more of it would bypass the bifurcation.

Flow into the hilar-cranial bronchus is net unidirectional, moving nearly twice as much air proximal as distal (Table 4), but not fully unidirectional. This means that the inspiratory aerodynamic valve is only partially effective in varanids. In birds, the intrapulmonary bronchus often narrows just before the opening to the secondary bronchi in a region called the *segmentum accelerans*, which is hypothesized to increase inspiratory flow of aerodynamic valving (Banzett et al., 1987; 1991; Maina and Africa, 2000). Previous CFD work on simplified ostrich lung models demonstrated only a moderate increase in the efficacy of aerodynamic valving due to a *segmentum accelerans* (Maina et al., 2009). Interestingly, this model predicted more complete inspiratory aerodynamic valving when more downstream features such as dorsal and secondary bronchi were included (Maina et al., 2009).

Interestingly, however, a widening in this region has been observed in *Columba livia* (Maina and Africa, 2000). In varanids, the intrapulmonary bronchus narrows just after the opening to the hilar-cranial bronchus, which may be responsible for air bypassing most of the next ostia (L1, M1, D1) during inspiration (Fig. 3F). Our results from the 3D printed models suggest that airway geometry and convective inertia are important mechanisms controlling flow in the hilar-cranial bronchus. It seems, however, that the airways are designed to employ high convective inertia as a mechanism for bypassing the hilar-cranial bronchus during expiration, but also keep it low during inspiration to cause tidal flow in the hilar-cranial bronchus. Our results also suggest that airway geometries downstream, as well as upstream, of the bifurcation affect aerodynamic valving. Proximal flow was not detected at any physiologically relevant flow rate during expiration in either modified print, suggesting that either decreasing the convective inertia via airway widening upstream (in the "Caudal Wide" model) or increasing the downstream resistance via airway

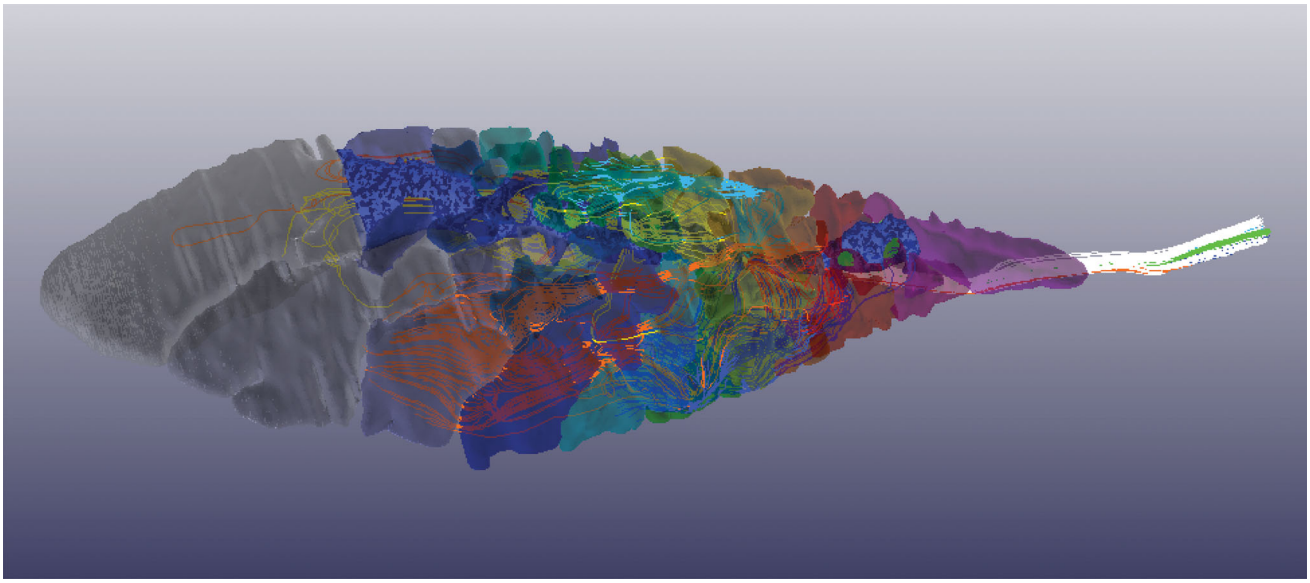

Fig. 21. Interactive 3D PDF of regional streamlines. Forward streamlines seeded from multiple locations in the lung model shown during mid-expiration (Time step 1), early inspiration (Time step 2), and late inspiration (Time step 3), and colored by seed location as described in Figure 14. Under 3D settings (accessible with a right click onto the activated 3D PDF) reduce the framerate threshold to 4 and select "None" under "optimization scheme for low framerate" for best results. Flash must be installed and enabled to view animations. 3D PDFs in the version of record are corrupted, but can be downloaded from https://tinyurl.com/LizardLungs.

widening downstream (in the "Cranial Narrow" model) was enough to prevent expiratory flow from traveling up into the hilar-cranial bronchus and even entrain flow from the hilar-cranial bronchus to flow out the intrapulmonary bronchus. In addition, the anatomically accurate airway geometry was most effective at shunting air up the hilar-cranial bronchus during inspiration in the dual-sensor measurements (Fig. 23), suggesting that the airway narrowing immediately caudal to the hilar-cranial bronchus ostia is at least partly responsible for generating tidal flow in the hilar-cranial bronchus.

Finally, these results raise questions about the effect of lung motion on intrapulmonary airflow. Varanids are unique among studied diapsids in using all of the dorsal ribs, including the floating ribs for ventilation (Cieri et al., 2018). In contrast, iguanas (Brainerd et al., 2016) and tegus (Capano et al., 2019) use primarily the true ribs that connect to the sternum for ventilation. Because varanid lungs differ from those of tegus or iguanas in having saccular lung chambers, the increased caudal rib motion may help to ventilate these chambers (Fig. 4). Duncker (1978) suggested that the caudal saccular

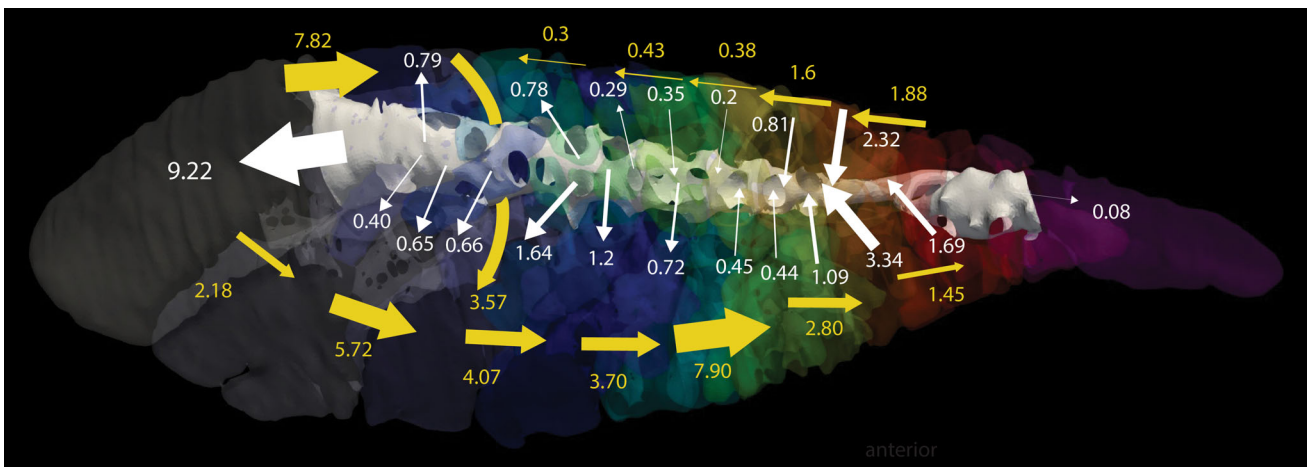

Fig. 22. Net flow in the lung of *V. exanthematicus*. Yellow arrows indicate the direction of simplified net intercameral transport. White arrows indicate direction of net transport between the intrapulmonary bronchus and the lateral, medial, and hilar-cranial secondary bronchi. Numbers refer to the amount of air in mL that is transported in the direction of the arrow during a ventilatory cycle. See Tables 1–5 and Figure 4 for details. In addition to the intracameral fluxes shown in the tables, 3.57 mL of air moves from the caudal medial chambers generally to the caudal lateral chambers ventral to the intrapulmonary bronchus during a ventilatory cycle.

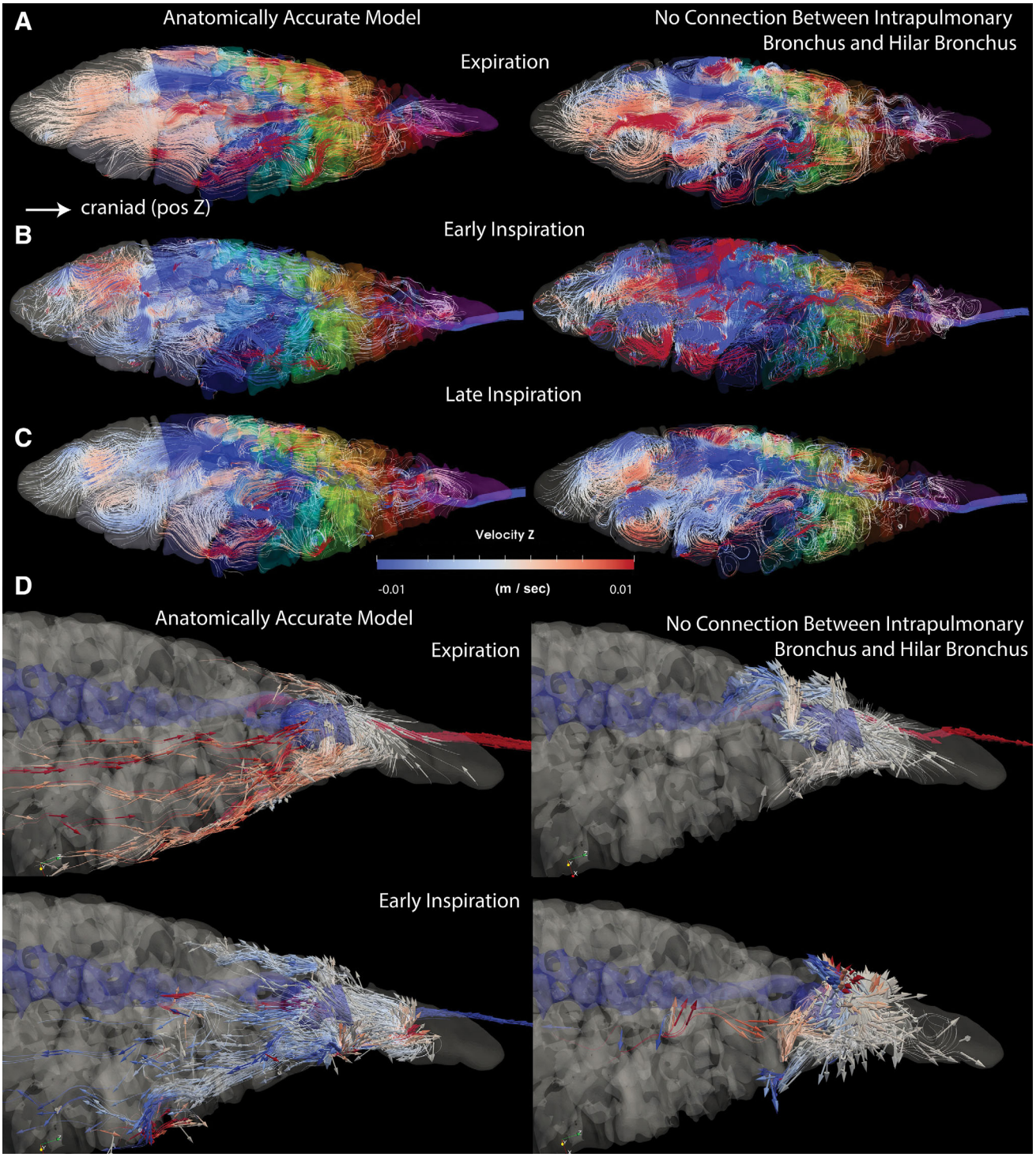

Fig. 23. Flow in modified CFD model without an ostium between the intrapulmonary bronchus and the hilar-cranial bronchus. Streamlines showing flow direction in the original anatomically accurate CFD model (left) and the model with closed-off ostium between the intrapulmonary bronchus and the hilar-cranial bronchus (right) during expiration (A), early inspiration (B), and late inspiration (C). Flow around the hilar-cranial bronchus is highlighted (D) showing flow during expiration (top) and early inspiration (bottom). Streamlines are colored by the cranial-caudal component of velocity where blue indicates caudal flow and red indicates cranial flow.

chambers are collapsed during normal respiration and are only engaged during certain behaviors, but fluoroscope recordings show that these chambers are often inflated during normal breathing (Klein and Owerkowicz, 2006; Cieri et al., 2018). Future CFD simulations that compare similar mesh motion amplitudes centered

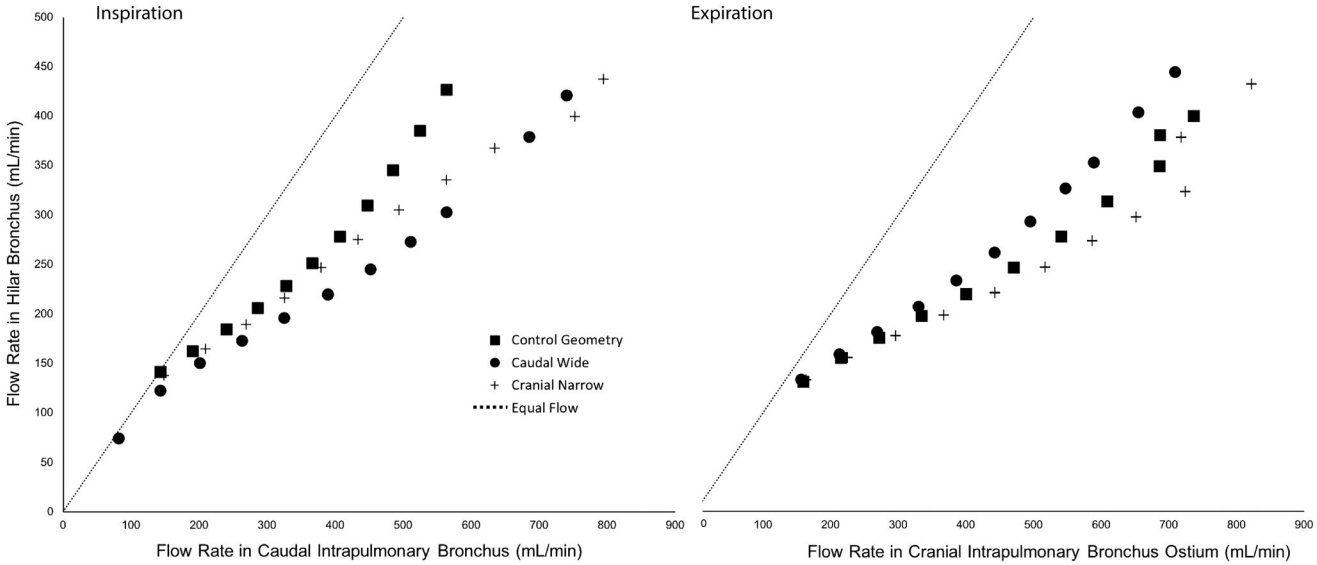

Fig. 24. The effect of geometry on the ratio of straight-branch (intrapulmonary bronchus) flow and side-branch (hilar-cranial bronchus) flow through 3D-printed bronchi models at varying input flow rates (see Fig. 5 and text for an explanation of the methods) during simulated inspiration (left) and simulated expiration (right) where thermistors were sealed to the models with dental impression material. Note that the flow scales are not identical. Input flow rates were 250–1,200 mL/min corresponding to Reynolds number range ~80–420 in the intrapulmonary bronchus at the location of the hilar-cranial bronchus ostium.

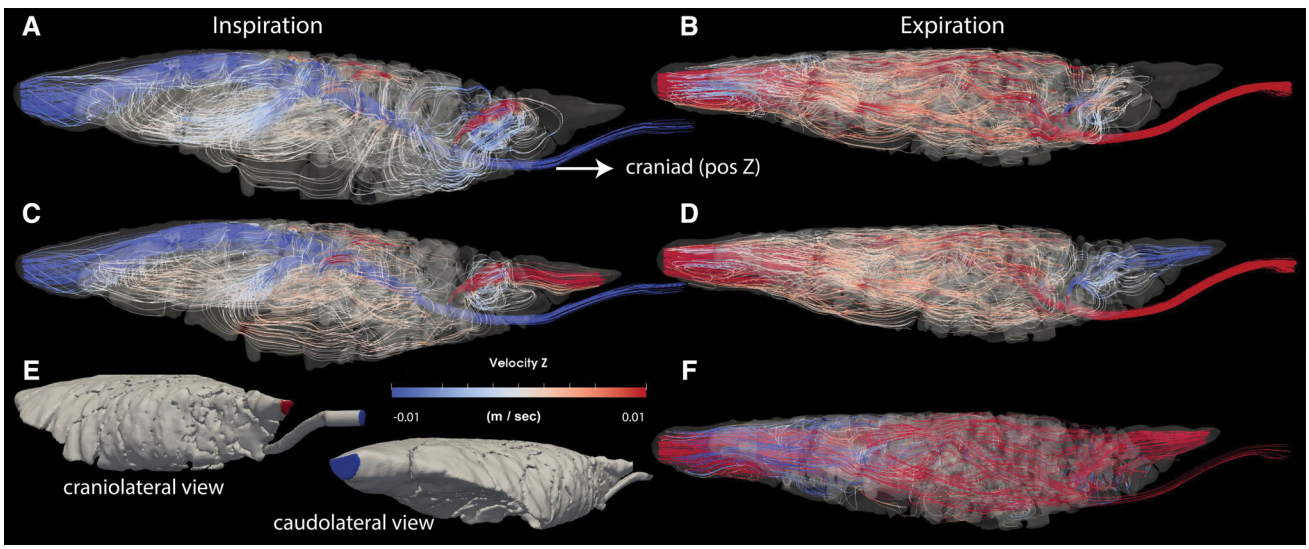

Fig. 25. Flow through steady-state CFD simulations where an additional outlet is placed at the cranial tip of the hilar-cranial bronchus. (A) Flow through the model when positive pressure is prescribed at the tracheal patch, the hilar-cranial patch is closed to flow, and zero pressure is prescribed at the caudal intrapulmonary bronchus patch to simulate inspiration. (B) Flow through the model when positive pressure is prescribed at the caudal intrapulmonary bronchus patch, the hilar-cranial patch is closed to flow, and zero pressure is prescribed at the tracheal patch to simulate expiration. (C) Flow through the model when positive pressure is prescribed at the tracheal patch and zero pressure is prescribed at the caudal intrapulmonary bronchus and hilar-cranial bronchus patches to simulate inspiration. (D) Flow through the model when positive pressure is prescribed at the hilar-cranial and caudal intrapulmonary bronchus patches and zero pressure is prescribed at the tracheal patch to simulate expiration. (E) Craniolateral and caudolateral views of the model geometry showing the tracheal boundary (blue) and the hilar-cranial bronchus boundary patch (red) inlet. (F) Flow through the model when positive pressure is prescribed at the caudal intrapulmonary bronchus patch and zero pressures are prescribed at the hilar-cranial and tracheal patches to simulate expiration. For all panels, streamlines are colored by the cranial-caudal component of velocity where blue indicates caudal flow and red indicates cranial flow.

around different regions of the lung should provide insight into the importance of saccular chambers and lung motion on pulmonary airflow.

Critique of the Methods

The CT scan on which the CFD simulation was based had a slice thickness of 600 μm, and there are undoubtedly lung anatomy features that were not resolved by the scan or eliminated during the segmentation, surface smoothing, and mesh generation algorithms, suggesting that the actual lung geometry may correspond to a model geometry intermediate between the control and the reduced intercameral perforation models. In addition, the boundary condition deformation field applied to the mesh to generate ventilation is an approximation of how the lung moves during ventilation. Thus, the CFD model does not faithfully represent all of the lung anatomy or completely faithful pulmonary motion but appears close enough to the real anatomy to provide accurate insight into macroscale pattern of flows, based on the flow validated with point measurements on excised lungs. The importance of the pattern of lung motion during ventilation to pulmonary airflow has yet to be investigated.

During model validation, it is possible that the presence of the probe changed the pattern of flow in the chamber in which it was placed, but the endoscope is so small that we consider this unlikely. Finally, measurements were made on excised and mechanically ventilated lungs and it is possible that patterns of airflow in lungs of intact, live-breathing animals are slightly different.

CONCLUSIONS

Although we are not suggesting that the lung of *V. exanthematicus* represents a transitional state, it has a unique airflow pattern that is an interesting blend of features similar to the bird and the iguana lung. Similar to the bird lung, inspired air travels net caudad through the center of the lung and net craniad through the walls connecting the chambers of the lungs. Also like the archosaur lung, the cranial chamber ostia are net incurrent and the caudal ostia off the intrapulmonary bronchus are net excurrent openings with respect to the intrapulmonary bronchus. The intercameral perforations in the varanid lung are similar to parabronchi of birds and even more like the intercameral perforations of crocodilians (Farmer, 2015b), in that they move air net cranially, but in monitors they are simple holes and not elaborate gas-exchange channels. The dorsal chambers and proximal aspects of the secondary bronchi, on the other hand, are similar to the avian parabronchi in that they are the sites of gas exchange. The density and distribution of intercameral perforations as well as lung morphology vary between varanid species (Becker et al., 1989) and future anatomical and CFD work should focus on this region of the respiratory system. On the other hand, both the varanid and the iguana lung feature a strong jet of air that bends flow cranially at the caudal aspect of the lung. In the varanid lung the inspiratory jet is central, and the return cranial flow is channeled through the lateral and medial secondary bronchi, whereas the caudal flow is lateral (though not completely touching the lateral walls), and the return flow is medial, spreading dorsally, and ventrally in the iguana. The net unidirectional scheme reported here may represent a possible evolutionary pathway for the evolution of the more complete unidirectional pulmonary airflow seen in crocodilians and birds. A varanid-style lung without intercameral perforations would necessarily be tidal, and a completely unidirectional lung could evolve from a varanid-style lung by increasing the amount of intercameral flow through more developed intercameral perforations. Study of more varanid species, which vary in the degree of intercameral perforation (Becker et al., 1989) or experimentation with CFD simulations based on varying meshes, may help to develop this line of thinking. Alternatively, the pulmonary pattern of pulmonary airflow of crocodilians and birds may also contain net unidirectionally with a temporary reversal of flow that was not detected by other methods. Future CFD simulations in these species based on high-fidelity digital meshes should facilitate better interspecific comparisons and reconstructions of tetrapod pulmonary patterns of airflow. These findings also raise the question of how different pulmonary airflow patterns relate to lung efficiency. Unfortunately, there is little data on nonavian reptiles and the comparisons of oxygen efficiency between mammals and birds, and nonavian reptiles are difficult because the latter breathe intermittently. Lung efficiency is commonly defined as oxygen extraction, which varies with the length of the breath hold (Cieri and Farmer, 2016). Although some varanid species have comparatively high maximal rates of oxygen consumption (Cieri et al., 2014), unidirectional pulmonary airflow is also present in green iguanas, which have much lower rates of maximal oxygen consumption (Wang et al., 1997). Other functional consequences for pulmonary airflow patterns, other than affecting maximal gas exchange rates, should be considered (Farmer, 2015c; Cieri and Farmer, 2016).

ACKNOWLEDGMENTS

The authors thank A. Summers, K. Cohen, and K. Hall for training and access to the micro-CT scanner used to visualize pulmonary circulation; B. Craven for mentoring in CFD; C. Lackey for assistance in segmenting CT data; M.W. Howell for assistance in 3D printing; and L.K. Hartzler for donating research specimens. The authors also thank A.M. Orendt and T.E. Cheatham at the Center for High Performance Computing, University of Utah as well as J.H. Kwack, M.W. Van Moer, and T. Cortese at the National Center for Supercomputing Applications for supercomputing and visualization support and for donating node hours to the project. This material is based upon work supported by the National Science Foundation Graduate Research Fellowship under Grant No. 1747505 and a Blue Waters Graduate Fellowship to R.L. Cieri and NSF Grant IOS-1055080 to C.G. Farmer. Any opinions, findings, and conclusions or recommendations expressed in this material are those of the authors and do not necessarily reflect the views of the National Science Foundation.

CONFLICT OF INTEREST

The authors declare no conflict of interest.

REFERENCES

Banzett RB, Butler JP, Nations CS, Barnas GM, Lehr JL, Jones JH. 1987. Inspiratory aerodynamic valving in goose lungs depends on gas density and velocity. Respir Physiol 70:287–300.

Banzett RB, Nations CS, Wang N, Fredberg JJ, Butler JP. 1991. Pressure profiles show features essential to aerodynamic valving in geese. Respir Physiol 84:295–309.

Becker H-O, Böhme W, Perry SF. 1989. Die Lungenmorphologie der Warane (Reptilia: Varanidae) und ihre systematisch-stammesgeschichtliche Bedeutung. Bonner Zool Beiträge 40:27–56.

Brainerd EL, Moritz S, Ritter DA. 2016. XROMM analysis of rib kinematics during lung ventilaiton in the green iguana, *Iguana iguana*. J Exp Biol 219:404–411.

Butler JP, Banzett RB, Fredberg JJ. 1988. Inspiratory valving in avian bronchi: aerodynamic considerations. Respir Physiol 72:241–255.

Capano JG, Moritz S, Cieri RL, Reveret L, Brainerd EL. 2019. Rib motions don't completely hinge on joint design: costal joint anatomy and ventilatory kinematics in a teiid lizard, *Salvator merianae*. Integr Org Biol 1:1–18.

Chiari Y, Cahais V, Galtier N, Delsuc F. 2012. Phylogenomic analyses support the position of turtles as the sister group of birds and crocodiles (Archosauria). BMC Biol 10:65.

Cieri RL, Craven BA, Schachner ER, Farmer CG. 2014. New insight into the evolution of the vertebrate respiratory system and the discovery of unidirectional airflow in iguana lungs. Proc Natl Acad Sci USA 111:17218–17223.

Cieri RL, Farmer CG. 2016. Unidirectional pulmonary airflow in vertebrates: a review of structure, function, and evolution. J Comp Physiol B 186:541–552.

Cieri RL, Moritz S, Capano JG, Brainerd EL. 2018. Breathing with floating ribs: XROMM analysis of lung ventilation in savannah monitor lizards. J Exp Biol 221:jeb.189449.

Duncker H-R. 1978. Coelom-Gliederung der Wirbeltiere-Funktionelle Aspekte. Verh Anat Ges 72:91–112.

Farmer CG. 2015a. Unidirectional flow in lizard lungs: a paradigm shift in our understanding of lung evolution in Diapsida. Fortschr Zool 188:299–301.

Farmer CG. 2015b. Similarity of crocodilian and avian lungs indicates unidirectional flow is ancestral for archosaurs. Integr Comp Biol 55:1–10.

Farmer CG. 2015c. The evolution of unidirectional pulmonary airflow. Phys Ther 30:260–272.

Farmer CG, Sanders K. 2010. Unidirectional airflow in the lungs of alligators. Science 327:338–340.

Heraty KB, Laffey JG, Quinlan NJ. 2008. Fluid dynamics of gas exchange in high-frequency oscillatory ventilation: in vitro investigations in idealized and anatomically realistic airway bifurcation models. Ann Biomed Eng 36:1856–1869.

Kirschfeld U. 1970. Eine Bauplanalyse der Waranlunge. Zool Beitraege NF 16:401–440.

Klein W, Owerkowicz T. 2006. Function of intracoelomic septa in lung ventilation of amniotes: lessons from lizards. Physiol Biochem Zool 79:1019–1032.

Lee MSY. 2001. Molecules, morphology, and the monophyly of diapsid reptiles. Contrib Zool 70:121–138.

Lyson TR, Sperling EA, Heimberg AM, Gauthier JA, King BL, Peterson KJ. 2012. MicroRNAs support a turtle + lizard clade. Biol Lett 8:104–107.

Maina JN. 2006. Development, structure, and function of a novel respiratory organ, the lung-air sac system of birds: to go where no other vertebrate has gone. Biol Rev Camb Philos Soc 81:545–579.

Maina JN, Africa M. 2000. Inspiratory aerodynamic valving in the avian lung: functional morphology of the extrapulmonary primary bronchus. J Exp Biol 203:2865–2876.

Maina JN, Maloiy GM, Warui CN, Njogu EK, Kokwaro ED. 1989. Scanning electron microscope study of the morphology of the reptilian lung: the Savanna monitor lizard *Varanus exanthematicus* and the pancake tortoise *Malacochersus tornieri*. Anat Rec 224:514–522.

Maina JN, Singh P, Moss EA. 2009. Inspiratory aerodynamic valving occurs in the ostrich, *Struthio camelus* lung: a computational fluid dynamics study under resting unsteady state inhalation. Respir Physiol Neurobiol 169:262–270.

Milani A. 1894. Beiträge zur Kenntniss der Reptilienlunge. I. Lacertilia. Zool Jahrbucher 10:93–146.

Owerkowicz T, Farmer CG, Hicks JW, Brainerd EL. 1999. Contribution of gular pumping to lung ventilation in monitor lizards. Science 284:1661–1663.

Perry SF. 1983. *Reptilian lungs: functional anatomy and evolution*. Springer-Verlag, Berlin Heidelberg.

Schachner ER, Cieri RL, Butler JP, Farmer CG. 2013b. Unidirectional pulmonary airflow patterns in the savannah monitor lizard. Nature 506:367–370.

Semple TL, Peakall R, Tatarnic NJ. 2019. A comprehensive and user-friendly framework for 3D-data visualisation in invertebrates and other organisms. J Morphol 280:223–231.

Wang N, Banzett RB, Butler JP, Fredberg JJ. 1988. Bird lung models show that convective inertia effects inspiratory aerodynamic valving. Respir Physiol 73:111–124.

Wang T, Carrier DR, Hicks JW. 1997. Ventilation and gas exchange in lizards during treadmill exercise. J Exp Biol 200:2629–2639.

Wolf S. 1933. Zur kenntnis von bau und funktion der reptilienlunge. Zollogische Jahrbucher 57:139–190.